# Quantitative Proteomics Using Stable Isotope Labeling with Amino Acids in Cell Culture Reveals Changes in the Cytoplasmic, Nuclear, and Nucleolar Proteomes in Vero Cells Infected with the Coronavirus Infectious Bronchitis Virus*[S]

**Edward Emmott‡§¶, Mark A. Rodgers‡‖, Andrew Macdonald‡, Sarah McCrory‡‖, Paul Ajuh**, and Julian A. Hiscox‡§‡‡**

**Virus-host interactions involve complex interplay between viral and host factors, rendering them an ideal target for proteomic analysis. Here we detail a high throughput quantitative proteomics analysis of Vero cells infected with the coronavirus infectious bronchitis virus (IBV), a positive strand RNA virus that replicates in the cytoplasm. Stable isotope labeling with amino acids in cell culture (SILAC) was used in conjunction with LC-MS/MS to identify and quantify 1830 cellular and two viral proteins from IBV-infected cells. Fractionation of cells into cytoplasmic, nuclear, and nucleolar extracts was used to reduce sample complexity and provide information on the trafficking of proteins between the different compartments. Each fraction showed a proportion of proteins exhibiting ≥2-fold changes in abundance. Ingenuity Pathway Analysis revealed that proteins that changed in response to infection could be grouped into different functional categories. These included proteins regulated by NF-κB- and AP-1-dependent pathways and proteins involved in the cytoskeleton and molecular motors. A luciferase-based reporter gene assay was used to validate the up-regulation of AP-1- and NF-κB-dependent transcription in IBV-infected cells and confirmed using immunofluorescence. Immunofluorescence was used to validate changes in the subcellular localization of vimentin and myosin VI in IBV-infected cells. The proteomics analysis also confirmed the presence of the viral nucleocapsid protein as localizing in the cytoplasm, nucleus, and nucleolus and the viral membrane protein in the cytoplasmic fraction. This research is the first application of SILAC to study total host cell proteome changes in response to positive sense RNA virus infection and illustrates the versatility of this technique as applied to infectious disease research.** ***Molecular & Cellular Proteomics 9:1920–1936, 2010.***

Virus infection and the host cell response involve a complex interplay of cellular and viral networks. Many viruses attempt to subvert host cell processes to increase the efficiency of virus infection, and likewise the cell utilizes a number of responses to generate an antiviral state. Previous studies have generally targeted defined cellular and viral pathways, and quantitative high throughput proteomics has not yet been applied widely to the study of virus infection in host cells. Coronaviruses are no exception to this, and infection has been demonstrated to result in the subversion of specific host cell processes, for example the cell cycle (1–4), apoptosis (5–7), and suppression of interferon (8, 9).

Coronaviruses generally cause respiratory and gastrointestinal infections in humans and animals. Examples include severe acute respiratory syndrome coronavirus (SARS-CoV),[1] which infects humans and animals (10), and infectious bronchitis virus (IBV), a disease of poultry that causes significant morbidity and mortality (11). Coronaviruses are characterized by having the largest positive sense single-stranded RNA genome in the virome and a replication process in the cytoplasm that involves discontinuous transcription during nega-

From the ‡Institute of Molecular and Cellular Biology, Faculty of Biological Sciences and the §Astbury Centre for Structural Molecular Biology, University of Leeds, Leeds LS2 9JT, United Kingdom and **Dundee Cell Products Ltd., James Lindsay Place, Dundee Technopole, Dundee DD1 5JJ, United Kingdom

Received, July 29, 2009, and in revised form, April 9, 2010

Published, MCP Papers in Press, May 13, 2010, DOI 10.1074/mcp.M900345-MCP200

[1] The abbreviations used are: SARS-CoV, severe acute respiratory syndrome coronavirus; AP-1, activator protein 1; ER, endoplasmic reticulum; IBV, infectious bronchitis virus; M, membrane; ERK, extracellular signal-regulated kinase; MAPK, mitogen-activated protein kinase; MYO6, myosin VI; N, nucleocapsid; NF-κB, nuclear factor κ B; PrV, pseudorabies virus; SILAC, stable isotope labeling with amino acids in cell culture; m.o.i., multiplicity of infection; Bis-Tris, 2-[bis(2-hydroxyethyl)amino]-2-(hydroxymethyl)propane-1,3-diol; IPI, International Protein Index; PEP, posterior error probability; FPR, false positive rate; DAPI, 4′,6-diamidino-2-phenylindole; PRDII, positive regulatory domain II.

tive strand synthesis (12). Thus, upon infection, the genome acts as a messenger RNA for the synthesis of the virus RNA replicase polyprotein, which then transcribes a nested set of virus subgenomic mRNAs and replicates genomic RNA. With some exceptions, the order of a gene along the coronavirus genome determines its mRNA abundance with the 3′-most genes (encoding the nucleocapsid (N) and membrane (M) proteins) having the most abundant mRNAs and the 5′-most genes (encoding the viral replicase) having the least abundant mRNAs. Viral protein abundance generally correlates with the abundance of the corresponding mRNA. Coronavirus replication is associated with membranes (13) and centered on double membrane vesicles that form in the cytoplasm of infected cells through the induction of autophagy (14, 15), a cellular stress response. Virus assembly occurs in the ER-Golgi intermediate compartment (16). As well as localizing to sites of replication, coronavirus proteins have been shown to target discrete cellular structures, such as the nucleolus (17) and mitochondria (18). In the case of the nucleolus, the observation of localization of a viral protein (N protein) to this structure was initially thought unusual given the site of viral RNA replication and that transcription of the virus is cytoplasmic. The N protein is a viral RNA-binding protein (19–21) and chaperone (22). However, many viruses target proteins to the nucleolus in many cases independent of the site of genome replication, and examples can be found from DNA, RNA, and retroviruses (23–25).

Proteomics has been applied to the interaction of coronaviruses with the host cell. For example, in SARS-CoV-infected cells, two-dimensional electrophoresis followed by ESI-MS/MS and isotope-coded affinity tag technology coupled to two-dimensional LC-MS/MS identified and quantified 355 proteins with 186 proteins showing a 1.5-fold or greater alteration between infected and mock-infected cells (26). In this study, high throughput quantitative proteomics using stable isotope labeling with amino acids in cell culture (SILAC) was used to investigate whether the Vero cell proteome changed in coronavirus-infected cells using IBV. Vero cells are commonly used in the propagation and study of many different animal and human pathogens, including SARS-CoV (27), respiratory syncytial virus (28), influenza virus (29), parainfluenza virus type 5 (30), and eukaryotic parasites (31). Vero cells are interferon-deficient and do not secret type 1 interferon when infected by viruses (they still have the interferon $\alpha/\beta$ receptor). However, this allows productive growth of pathogens and infection and reduces the bystander effect in uninfected cells. Given their common use in investigating host-pathogen interactions, antiviral screening (32), and vaccine production (33), a map of the Vero cell proteome is advantageous. To reduce sample complexity and to study the interaction of IBV with different regions of the Vero cell, the cytoplasmic, nuclear, and nucleolar proteomes were analyzed. Many cellular proteins were shown to increase and decrease in abundance in response to IBV infection. Bioinformatic analyses of protein networks and pathways predicted that signaling cascades could be induced in IBV-infected cells, and this was validated experimentally. To our knowledge, this research is the first application of SILAC to study total host cell proteome changes in response to positive sense RNA virus infection and illustrates the versatility of this technique as applied to infectious disease research.

## EXPERIMENTAL PROCEDURES

*Virus and Cells*—Vero cells were grown at 37 °C with 5% $CO_2$ in Dulbecco's modified Eagle's medium supplemented with 10% fetal calf serum and penicillin/streptomycin. IBV (Beaudette-United States strain) was propagated in Vero cells, and the virus was harvested at 24 h postinfection. Virus titer was calculated by plaque assay titration in Vero cells. For SILAC experiments, cells were grown in media containing either unlabeled arginine and lysine amino acids (R0K0) or containing $^{13}$C-labeled arginine and lysine amino acids (R6K6) and supplemented with 10% dialyzed fetal calf serum and penicillin/streptomycin for 10 rounds of cell division. Cells were then grown in 500-cm$^2$ dishes until 60% confluent and infected with virus/mock-infected at a multiplicity of infection (m.o.i.) of 1. All cells were confirmed to be *Mycoplasma*-free.

*Cellular Fractionation into Cytoplasmic, Nuclear, and Nucleolar Fractions*—Cellular fractionation was carried out as in Andersen *et al.* (34) with the number of sonication repeats increased to 10 repeats of 10 s on, 10 s off.

*Gel Electrophoresis and In-gel Digestion*—Each sample was reduced in SDS-PAGE loading buffer containing 10 mM DTT and alkylated in 50 mM iodoacetamide prior to being boiled, then separated by one-dimensional SDS-PAGE (4–12% Bis-Tris Novex minigel, Invitrogen), and visualized by colloidal Coomassie staining (Novex, Invitrogen). The entire protein gel lane was excised and cut into 10 gel slices each. Every gel slice was subjected to in-gel digestion with trypsin (35). The resulting tryptic peptides were extracted by 1% formic acid, acetonitrile; lyophilized in a SpeedVac (Helena Biosciences); and resuspended in 1% formic acid.

*LC-MS/MS*—Trypsin-digested peptides were separated using an Ultimate U3000 (Dionex Corp.) nanoflow LC system consisting of a solvent degasser, micro- and nanoflow pumps, flow control module, UV detector, and a thermostated autosampler. 10 ml of sample (a total of 2 mg) was loaded with a constant flow of 20 ml/min onto a PepMap $C_{18}$ trap column (0.3-mm inner diameter × 5 mm; Dionex Corp.). After trap enrichment, peptides were eluted off onto a PepMap $C_{18}$ nanocolumn (75 mm × 15 cm; Dionex Corp.) with a linear gradient of 5–35% solvent B (90% acetonitrile with 0.1% formic acid) over 65 min with a constant flow of 300 nl/min. The HPLC system was coupled to an LTQ Orbitrap XL (Thermo Fisher Scientific Inc.) via a nano-ES ion source (Proxeon Biosystems). The spray voltage was set to 1.2 kV, and the temperature of the heated capillary was set to 200 °C. Full-scan MS survey spectra (*m/z* 335–1800) in profile mode were acquired in the Orbitrap with a resolution of 60,000 after accumulation of 500,000 ions. The five most intense peptide ions from the preview scan in the Orbitrap were fragmented by collision-induced dissociation (normalized collision energy, 35%; activation Q, 0.250; and activation time, 30 ms) in the LTQ after the accumulation of 10,000 ions. Maximal filling times were 1000 ms for the full scans and 150 ms for the MS/MS scans. Precursor ion charge state screening was enabled, and all unassigned charge states as well as singly charged species were rejected. The dynamic exclusion list was restricted to a maximum of 500 entries with a maximum retention period of 90 s and a relative mass window of 10 ppm. The lock mass option was enabled for survey scans to improve mass accuracy (36). The data were acquired using Xcalibur software.

*Quantification and Bioinformatics Analysis*—Quantification was performed with MaxQuant version 1.0.7.4 (37) and was based on two-dimensional centroid of the isotope clusters within each SILAC pair. To minimize the effect of outliers, protein ratios were calculated as the median of all SILAC pair ratios that belonged to peptides contained in the protein. The percentage of variability of the quantitation was defined as the standard deviation of the natural logarithm of all ratios used for obtaining the protein ratio multiplied by a constant factor of 100.

The generation of the peak list, SILAC- and extracted ion current-based quantitation, calculated posterior error probability and false discovery rate based on search engine results, peptide to protein group assembly, and data filtration and presentation were carried out using MaxQuant. The derived peak list was searched with the Mascot search engine (version 2.1.04; Matrix Science, London, UK) against a concatenated database combining 80,412 proteins from the International Protein Index (IPI) human protein database version 3.6 (forward database) and the reversed sequences of all proteins (reverse database). Alternatively, database searches were done using Mascot (Matrix Science) as the database search engine, and the results were saved as a peptide summary before quantification using MSQuant (SourceForge). Parameters allowed included up to three missed cleavages and three labeled amino acids (arginine and lysine). Initial mass deviation of precursor ions and fragment ions were up to 7 ppm and 0.5 Da, respectively. The minimum required peptide length was set to 6 amino acids. To pass statistical evaluation, posterior error probability (PEP) for peptide identification (MS/MS spectra) should be below or equal to 0.1. The required false positive rate (FPR) was set to 5% at the peptide level. False positive rates or PEPs for peptides were calculated by recording the Mascot score and peptide sequence length-dependent histograms of forward and reverse hits separately and then using Bayes' theorem to derive the probability of a false identification for a given top scoring peptide. At the protein level, the false discovery rate was calculated as the product of the PEP of the peptides of a protein where only peptides with distinct sequences were taken into account. If a group of identified peptide sequences belongs to multiple proteins and these proteins cannot be distinguished with no unique peptide reported, these proteins are reported as a protein group in MaxQuant. Proteins were quantified if at least one MaxQuant-quantifiable SILAC pair was present. Identification was set to a false discovery rate of 1% with a minimum of two quantifiable peptides. The set value for FPR/PEP at the peptide level ensures that the worst identified peptide has a probability of 0.05 of being false, and proteins are sorted by the product of the false positive rates of their peptides where only peptides with distinct sequences are recognized. During the search, proteins are successively included starting with the best identified proteins until a false discovery rate of 1% is reached, an estimation based on the fraction of reverse protein hits. Enzyme specificity was set to trypsin allowing for cleavage N-terminal to proline and between aspartic acid and proline. Carbamidomethylation of cysteine was searched as a fixed modification, whereas *N*-acetyl protein and oxidation of methionine were searched as variable modifications.

*Protein Pathway Analysis*—Data were analyzed through the use of Ingenuity Pathways Analysis (Ingenuity® Systems). Networks were generated using data sets containing gene identifiers and corresponding expression values and uploaded into the application. Each gene identifier was mapped to its corresponding gene object in the Ingenuity Pathways Knowledge Base. A cutoff of 2.0 was set to identify genes whose expression was significantly differentially regulated. These genes, called focus genes, were overlaid onto a global molecular network developed from information contained in the Ingenuity Pathways Knowledge Base. Networks of these focus genes were then algorithmically generated based on their connectivity. Graphical representations of the molecular relationships between genes/gene products were generated. Genes or gene products are represented as nodes, and the biological relationship between two nodes is represented as an edge (line). All edges are supported by at least one reference from the literature or from canonical information stored in the Ingenuity Pathways Knowledge Base. Human, mouse, and rat orthologs of a gene are stored as separate objects in the Ingenuity Pathways Knowledge Base but are represented as a single node in the network. The intensity of the node color indicates the degree of up- (red) or down (green)-regulation. Nodes are displayed using various shapes that represent the functional class of the gene product.

*Confocal Microscopy*—Coverslips containing fixed samples were mounted onto slides using Vectorshield containing DAPI (Vector Laboratories) to allow visualization of cell nuclei. Confocal images were captured on an LSM510 META microscope (Carl Zeiss Ltd.) equipped with 40× and 63×, numerical aperture 1.4, oil immersion lenses. Pinholes were set to allow optical sections of 1 $\mu$m to be acquired. All fluorescence was measured in the linear range as the detector is a photomultiplier, and the range indicator was utilized to ensure that no saturated pixels were obtained on image capture. Images were averaged eight times. Live cell work was conducted as described (38).

*Western Blot*—Cellular fractions were obtained as detailed above. Total protein was assayed by BCA assay (Pierce). 5 mg of protein was resolved by 12% SDS-PAGE and transferred to PVDF membranes (Millipore) using a Bio-Rad semidry transfer apparatus. ECL detection was used to detect proteins.

*Antibodies*—IBV proteins were detected with chicken anti-IBV polyclonal serum (1:20,000; Charles River). Anti-RelA, -p50, -nucleolin, -fibrillarin, -myosin VI, and -tubulin antibodies were obtained from Abcam, and anti-lamin B was from Calbiochem. The anti-vimentin antibody was a kind donation from Tom Wileman (University of East Anglia). Horseradish peroxidase-conjugated secondary antibodies for Western blotting were obtained from Sigma, and Alexa Fluor-conjugated secondary antibodies (A488 and A568) were obtained from Molecular Probes (Invitrogen).

*Assay for Induction of AP-1*—80% confluent cell monolayers in 12-well dishes were co-transfected with 100 ng of AP-1 reporter plasmid and 10 ng of *Renilla* reporter plasmid per well using Lipofectamine 2000 (Invitrogen) according to the manufacturer's protocol in serum-free media. After 24-h incubation, the transfection mixture was replaced with either plain PBS (mock), IBV in PBS (m.o.i. of 5), or Sendai virus in PBS (100 hemagglutinin units/well). Plates were then rocked at 37 °C for 1 h before PBS was replaced with 400 $\mu$l of full media and incubated at 37 °C for 24 h. Cells were lysed and harvested according to the Promega Dual-Luciferase kit for the luciferase assay. Control plates of transfection mixture only and media only were included to rule out background reactivity (data not shown).

*Assay for Detection of NF-κB*—80% confluent cell monolayers in 12-well dishes were co-transfected with 100 ng of NF-κB or positive regulatory domain II (PRDII) reporter plasmid and 10 ng of *Renilla* reporter plasmid per well using Lipofectamine 2000 (Invitrogen) in serum-free media according to the manufacturer's instructions. After 24-h incubation, the transfection mixture was replaced with either plain PBS (mock), IBV in PBS (m.o.i. of 5), or Sendai virus in PBS (100 hemagglutinin units/well). Plates were then rocked at 37 °C for 1 h before PBS was replaced with 400 $\mu$l of full media and incubated at 37 °C for 24 h with 5% $CO_2$. Cells were lysed and harvested according to the Promega Dual-Luciferase kit for the luciferase assay. Control plates of transfection mixture only and media only were included to rule out background reactivity (data not shown).

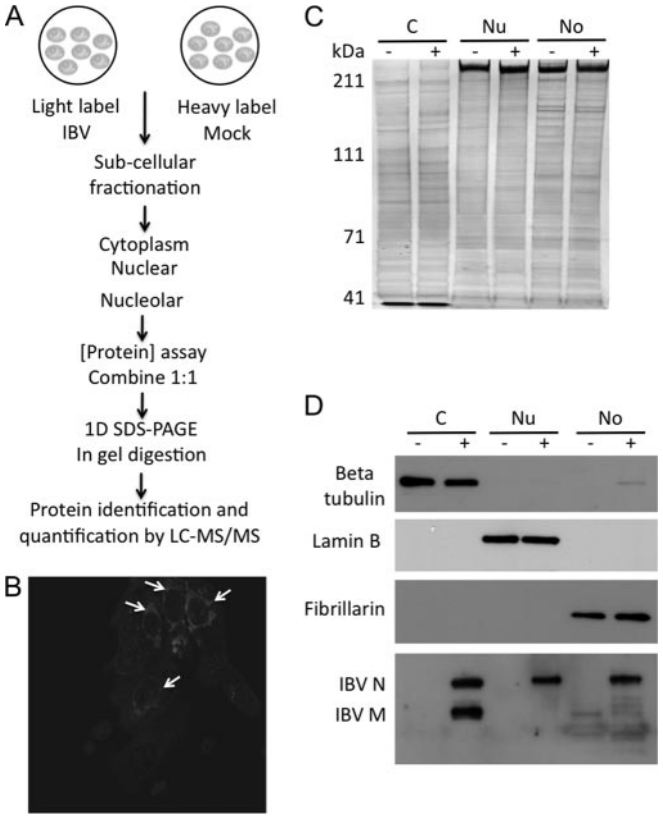


FIG. 1. *A*, diagrammatic representation of the high throughput quantitative experimental approach taken in this study to investigate changes in the cellular proteome in response to infection with IBV. *B*, immunofluorescence analysis using confocal microscopy of IBV-infected cells, examples of which are marked with *arrows*. *C*, cytoplasmic (*C*), nuclear (*Nu*), and nucleolar (*No*) proteomes purified from mock- (−) and IBV-infected (+) cells. Molecular mass is shown to the *left*. *D*, Western blot analysis of the cytoplasmic (*C*), nuclear (*Nu*), and nucleolar (*No*) extracts using antibodies to specific markers for each fraction, tubulin-1 for the cytoplasm, lamin B-1 for the nucleus, and fibrillarin for the nucleolus.

Cytoplasmic N protein (Mascot score 1064), peptide coverage 59%.

MASGKAAGK***TDAPAPVIKLGGPKPPKVGSSGNASWFQAIK***AK***KLNTPPPKFEGSGVPDNENIKPSQQHGYWR***RQARFKPGKG
GRKPVPDAWYFYYTGTGPAADLNWGDTQDGIVWVAAKGADTKSRSNQGTR***DPDKFDQYPLRFSDGGPDGNFRWDFIPLNR***GR
SGR***STAASSAAASR***APSREGSGRGR***RSDSGDDLIAR***AAK***IIQDQQK***KGSRITK***AKADEMAHR***RYCKRTIPPNYR***VDQVFGPR***T
KGKEGNFGDDK***MNEEGIKDGRVTAMLNLVPSSHACLFGSR***VTPK***LQLDGLHLRFEFTTVVPCDDPQFDNYVKICDQCVDGVG
***TRPK***DDEPKPKSRSSSRPATRGNSPAPRQQRPKKEKKLKKQDDEADK***ALTSDEERNNAQLEFYDEPKVINWGDAALGENEL***

Nuclear N protein (Mascot score 900), peptide coverage 58%.

MASGKAAGK***TDAPAPVIKLGGPKPPKVGSSGNASWFQAIK***AK***KLNTPPPKFEGSGVPDNENIKPSQQHGYWR***RQARFKPGKG
GRKPVPDAWYFYYTGTGPAADLNWGDTQDGIVWVAAKGADTKSRSNQGTR***DPDKFDQYPLRFSDGGPDGNFRWDFIPLNR***GR
***SGRSTAASSAAASR***APSREGSGRGR***RSDSGDDLIAR***AAK***IIQDQQK***KGSRITK***AKADEMAHR***RYCKRTIPPNYR***VDQVFGPR***T
KGKEGNFGDDK***MNEEGIKDGRVTAMLNLVPSSHACLFGSR***VTPK***LQLDGLHLRFEFTTVVPCDDPQFDNYVKICDQCVDGVG
***TRPK***DDEPKPKSRSSSRPATRGNSPAPRQQRPKKEKKLKKQDDEADKALTSDEER***NNAQLEFYDEPKVINWGDAALGENEL***

Nucleolar N protein (Mascot score 429), peptide coverage 40%.

MASGKAAGKTDAPAPVIKLGGPKPPK***VGSSGNASWFQAIK***AK***KLNTPPPKFEGSGVPDNENIKPSQQHGYWR***RQARFKPGKG
GRKPVPDAWYFYYTGTGPAADLNWGDTQDGIVWVAAKGADTKSRSNQGTR***DPDKFDQYPLRFSDGGPDGNFR***WDFIPLNRGR
SGRSTAASSAAASRAPSREGSGRGR***RSDSGDDLIAR***AAKIIQDQQKKGSRITK***AKADEMAHRR***YCKRTIPPNYR***VDQVFGPR***T
KGK***EGNFGDDKMNEEGIKDGRVTAMLNLVPSSHACLFGSR***VTPKLQLDGLHLR***FEFTTVVPCDDPQFDNYVKICDQCVDGVG***
***TRPK***DDEPKPKSRSSSRPATRGNSPAPRQQRPKKEKKLKKQDDEADKALTSDEERNNAQLEFYDEPKVINWGDAALGENEL

Cytoplasmic M protein (Mascot score 129), peptide coverage 12%.

MPNETNCTLDFEQSVQLFKEYNLFITAFLLFLTIILQYGYATRTKVIYTLKMIVLWCFWPLNIAVGVISCTYPPNTGGLVVA
IILTVFACLSFVGYWIQSIRLFKRCRSWWSFNPESNAVGSILLTNGQQCNFAIESVPMVLSPIIKNGVLYCEGQWLAKCEPD
HLPKDIFVCTPDRRNIYRMVQKYTGDQSGNKKR***FATFVYAKQSVDTGELESVATGGSSLYT***

FIG. 2. **Amino acid sequence of IBV N and M protein sequences showing peptide coverage (*bold* and *italic*) on proteins identified from nuclear, cytoplasmic, and nucleolar extracts.** Mascot score and percent peptide coverage are provided.

RESULTS

Quantitative high throughput proteomics analysis using SILAC (Fig. 1*A*) was used to investigate the potential changes in the Vero cell proteome in response to IBV infection (Fig. 1*B*). To reduce sample complexity, maximize protein coverage, and reflect where different proteins can traffic, the cell was fractionated into samples enriched in cytoplasmic, nuclear, and nucleolar proteins (Fig. 1*C*). These samples were validated using antibodies to known cellular and viral proteins that were enriched in each fraction (Fig. 1*D*). β-Tubulin, a cytoplasmic marker protein, was present in the cytoplasmic fractions, absent in the nuclear fractions, but enriched in the nucleolar fraction from IBV-infected cells. Lamin B and fibrillarin, markers for the nucleus and nucleolus, respectively, were detected in their respective fractions. The IBV N protein was detected in all fractions prepared from infected cells. The viral M protein was present in the cytoplasmic fraction only. No proteins corresponding to the known molecular weights of viral proteins were detected in fractions prepared from mock-infected cells. In total, 1830 cellular proteins were both identified and quantified by LC-MS/MS. These were divided between the cytoplasmic (818 proteins; supplemental Table 1), nuclear (506 proteins; supplemental Table 2), and nucleolar fractions (506 proteins; supplemental Table 3). Where only single peptides hits were obtained for proteins, spectra have been included (supplemental Fig. 1). Also, for the nucleolar proteome, proteins identified by single peptides were included only if they were present in the human nucleolar proteome database (52). Two viral proteins were detected in this analysis, the N and the M proteins. The N protein was identified in the nuclear, cytoplasmic, and nucleolar proteomes, and the M protein was identified in the cytoplasm only (Fig. 2) and validated the Western blot data presented in Fig. 1*D*.

For quantitative analysis, previous investigations using SILAC have applied ratio cutoffs ranging from near 1.0- to 2-fold (39, 40). An analysis investigating changes in cellular proteins in SARS-CoV-infected cells by two-dimensional gel electrophoresis used a ratio of 1.5-fold as a basis for comparison (26). In this study, a 2.0-fold cutoff was used to identify proteins whose abundance may have changed in IBV-infected cells. However, as can be seen from Fig. 1*B*, not all cells were infected with IBV. A known feature of IBV infection is that virus spreads through initiating new foci of infection and cell-to-cell fusion (41). Thus, infection is not synchronous, and not all cells will be infected. Hence, changes in the cellular proteome in response to IBV infection in cell culture may be under-representative of what is occurring in an individual cell. Comparison between the mock- and IBV-infected cells indicated for all three proteomes that certain proteins changed in abundance. In the cytoplasmic proteome, one protein (0.1%) showed ≥2.0-fold reduction in the cytoplasm of IBV-infected cells, and 66 proteins (8.1%) showed a ≥2.0-

TABLE I

*Cytoplasmic proteins identified by LC-MS/MS demonstrating ≥2-fold change in abundance in response to IBV infection*

Notes on protein function were obtained from annotations in the UniProt database. ssDNA, single-stranded DNA; dsDNA, double-stranded DNA.

| Protein ID | Name | Ratio | Peptides | Sequence coverage | PEP | Function |
|---|---|---|---|---|---|---|
| | | | | % | | |
| Proteins present in increased abundance in IBV-infected cells | | | | | | |
| IPI00299554 | KIF14 | 121.5 | 13 | 0.7 | 0.030844 | Essential for cytokinesis |
| IPI00910009 | cDNA FLJ53554 | 119.4 | 15 | 6.6 | 0.017233 | Unknown |
| IPI00152881 | Shroom3 | 21.8 | 7 | 0.5 | 0.021639 | Cell morphology |
| IPI00289501 | VGF | 4.4 | 5 | 10.4 | $3.51 \times 10^{-11}$ | Regulation of cell-cell interactions |
| IPI00902514 | Histone H2A | 4.3 | 3 | 11.2 | 0.013631 | DNA binding, nucleosome component |
| IPI00876941 | Caveolin 1 variant | 4.1 | 3 | 13.4 | $6.75 \times 10^{-11}$ | A scaffolding protein within caveolar membranes |
| IPI00418471 | Vimentin | 3.6 | 137 | 63.7 | $9.49 \times 10^{-297}$ | Cytoskeleton |
| IPI00004669 | pp-GaNTase 2 | 3.4 | 2 | 4.4 | 0.001276 | *O*-Linked glycosylation |
| IPI00220739 | mPR | 3.2 | 3 | 14.9 | $2.37 \times 10^{-17}$ | Progesterone receptor |
| IPI00218466 | SEC61A1 | 3.0 | 2 | 6 | 0.001145 | Insertion of membrane or secretory proteins into the ER |
| IPI00102069 | eIF 3 | 3.0 | 3 | 10.2 | $6.86 \times 10^{-9}$ | Protein synthesis |
| IPI00910513 | cDNA FLJ78119 | 3.0 | 3 | 4.4 | 0.004264 | Highly similar to *Homo sapiens* $G_1$ to S phase transition 1 |
| IPI00855785 | Fibronectin | 2.9 | 8 | 3.7 | $2.07 \times 10^{-34}$ | Cell adhesion, cell morphology |
| IPI00166293 | Histone H2B type 3-B | 2.9 | 10 | 35.7 | $7.54 \times 10^{-36}$ | DNA binding, nucleosome component |
| IPI00296190 | C10orf58 | 2.8 | 2 | 10 | 0.003213 | Unknown |
| IPI00010951 | Epiplakin | 2.8 | 2 | 3.7 | $1.51 \times 10^{-21}$ | Cytoskeleton |
| IPI00328319 | RBBP4 | 2.7 | 2 | 9.4 | $5.23 \times 10^{-20}$ | Chromatin remodeling |
| IPI00019353 | Acylglycerol kinase | 2.7 | 2 | 11.1 | 0.008944 | Lipid kinase |
| IPI00232533 | eIF 1A | 2.6 | 3 | 11.8 | 0.001923 | Protein biosynthesis |
| IPI00017726 | Type II HADH | 2.6 | 2 | 12.3 | 0.000319 | Mitochondrial tRNA maturation |
| IPI00398002 | Plectin-1 | 2.6 | 216 | 30.5 | 0 | Structural/regulatory component of cytoskeleton |
| IPI00030847 | TM9SF3 | 2.5 | 3 | 6.3 | $7.02 \times 10^{-29}$ | Unknown |
| IPI00025831 | CYP3A5 | 2.5 | 4 | 8.6 | $7.24 \times 10^{-28}$ | Oxidation of a variety of compounds |
| IPI00013122 | p50Cdc37 | 2.5 | 2 | 5.6 | $8.13 \times 10^{-8}$ | Promotes kinase interaction with the HSP90 complex |
| IPI00847322 | Superoxide dismutase | 2.5 | 8 | 42.8 | $4.65 \times 10^{-60}$ | Removal of oxygen radicals |
| IPI00554788 | Keratin | 2.4 | 16 | 21.4 | $9.04 \times 10^{-84}$ | Filament reorganization |
| IPI00642584 | KIAA0090 | 2.4 | 2 | 2.9 | 0.001148 | Unknown |
| IPI00294840 | AIM1 | 2.3 | 3 | 2.7 | $2.50 \times 10^{-8}$ | Interacts with cytoskeleton |
| IPI00024976 | hTom22 | 2.3 | 3 | 31 | 3.03E-06 | Import of cytoplasmic mitochondrial proteins |
| IPI00759493 | cDNA FLJ76284 | 2.3 | 2 | 9 | 0.004796 | Unknown |
| IPI00237884 | AKAP 250 | 2.3 | 3 | 0.8 | $2.69 \times 10^{-7}$ | Anchoring protein for protein kinases A and C |
| IPI00021695 | PMCA1 | 2.3 | 3 | 3.7 | $9.83 \times 10^{-17}$ | Calcium export |
| IPI00465432 | Nodal modulator 2 | 2.2 | 4 | 4.3 | 0.000351 | Nodal signaling |
| IPI00026970 | hSPT16 | 2.2 | 5 | 4.8 | $6.53 \times 10^{-5}$ | Nucleosome reorganization |
| IPI00027175 | Sorcin | 2.2 | 2 | 11.1 | 0.000415 | Calcium ion binding |
| IPI00220487 | ATP5H | 2.2 | 11 | 44.1 | $6.23 \times 10^{-15}$ | ATP synthesis |
| IPI00873223 | cDNA FLJ56155 | 2.2 | 2 | 4.6 | $6.81 \times 10^{-12}$ | Nucleotidyltransferase activity |
| IPI00020557 | LRP | 2.1 | 2 | 0.6 | $6.32 \times 10^{-6}$ | Involved in endocytosis, phagocytosis, cell growth |
| IPI00003269 | κ-Actin | 2.1 | 6 | 14.1 | $1.00 \times 10^{-19}$ | Cytoskeleton, cell motility |
| IPI00005537 | L12mt | 2.1 | 4 | 18.2 | $3.92 \times 10^{-9}$ | Mitochondrial ribosome component |
| IPI00156689 | VAT1 | 2.1 | 6 | 14.8 | $1.04 \times 10^{-22}$ | Zinc ion binding, oxidoreductase activity |
| IPI00017283 | IleRS | 2.1 | 5 | 4.5 | 0.000219 | Isoleucine-tRNA ligase |
| IPI00018783 | ITPase | 2.1 | 2 | 19.1 | 0.000154 | Nucleotide metabolism |
| IPI00334190 | SLP-2 | 2.1 | 6 | 33.7 | $4.23 \times 10^{-73}$ | Associated with the cytoskeleton |
| IPI00008982 | P5CS | 2.1 | 4 | 3 | $9.05 \times 10^{-19}$ | Proline biosynthesis |
| IPI00219097 | HMG-2 | 2.1 | 2 | 7.2 | 0.00367 | Binds ssDNA and unwinds dsDNA |
| IPI00215719 | RPL18 | 2.1 | 2 | 12.8 | $3.42 \times 10^{-7}$ | Large ribosome subunit |
| IPI00386271 | SLC25A12 | 2.1 | 5 | 11.1 | $2.05 \times 10^{-18}$ | Calcium-dependent mitochondrial aspartate and glutamate carrier |
| IPI00014424 | eEF1A-2 | 2.1 | 8 | 50.5 | $5.11 \times 10^{-90}$ | Protein biosynthesis |

TABLE I—*continued*

| Protein ID | Name | Ratio | Peptides | Sequence coverage | PEP | Function |
|---|---|---|---|---|---|---|
| IPI00010845 | CI-23kD | 2.1 | 2 | 4.3 | 0.004255 | Core subunit of the mitochondrial membrane respiratory chain |
| IPI00554481 | 4F2hc | 2.1 | 4 | 4.8 | $2.29 \times 10^{-13}$ | Amino acid transport, required for cell growth |
| IPI00015476 | ASCT1 | 2.0 | 3 | 4.9 | 0.001305 | Sodium-dependent amino acid transport |
| IPI00296337 | DNPK1 | 2.0 | 18 | 5.8 | $1.01 \times 10^{-53}$ | Sensor for DNA damage and functions in DNA repair |
| IPI00003925 | PDHE1-B | 2.0 | 6 | 17.3 | $3.61 \times 10^{-14}$ | Conversion of pyruvate to acetyl-CoA and $CO_2$ |
| IPI00022793 | TP-$\beta$ | 2.0 | 4 | 8.6 | $1.50 \times 10^{-12}$ | Fatty acid oxidation |
| IPI00419258 | HMG-1 | 2.0 | 8 | 21.9 | $1.19 \times 10^{-7}$ | Binds ssDNA and unwinds dsDNA |
| IPI00029264 | Cytochrome $c_1$ | 2.0 | 2 | 8.9 | $4.24 \times 10^{-6}$ | Mitochondrial respiratory chain |
| IPI00299571 | PDIA6 | 2.0 | 13 | 20.7 | $1.72 \times 10^{-65}$ | Catalyzes the rearrangement of disulfide bonds |
| IPI00011253 | 40 S ribosomal protein S3 | 2.0 | 15 | 50.6 | $1.30 \times 10^{-18}$ | Ribosomal protein |
| IPI00029737 | LACS 4 | 2.0 | 15 | 23.5 | $9.19 \times 10^{-33}$ | Synthesis of cellular lipids and degradation via $\beta$-oxidation |
| IPI00021338 | PDC-E2 | 2.0 | 5 | 6.2 | 0.000723 | Catalyzes the conversion of pyruvate to acetyl-CoA and $CO_2$ |
| IPI00328415 | B5R | 2.0 | 5 | 14.6 | $2.29 \times 10^{-15}$ | Desaturation and elongation of fatty acids, cholesterol biosynthesis |
| IPI00014230 | gC1qBP | 2.0 | 3 | 12.4 | $2.44 \times 10^{-20}$ | Immune response, complement activation |
| IPI00021048 | Myoferlin | 2.0 | 12 | 5.4 | $2.37 \times 10^{-42}$ | Plasma membrane repair |
| IPI00871843 | TGM2 | 2.0 | 3 | 4.9 | $2.12 \times 10^{-8}$ | Catalyzes protein cross-linking, polyamine-protein conjugation |
| IPI00513768 | ATAD3C | 2.0 | 13 | 3.9 | 0.003615 | Nucleoside triphosphatase activity |
| Proteins present in decreased abundance in IBV-infected cells | | | | | | |
| IPI00873829 | ACAA2 | 5.2 | 2 | 7.8 | $9.51 \times 10^{-9}$ | Acyltransferase |

fold increase in the cytoplasm of IBV-infected cells (Table I). In the nuclear proteome, 35 proteins (6.9%) showed ≥2.0-fold reduction in the nucleus of IBV-infected cells, and five proteins (1.0%) showed ≥2.0-fold increase in the nucleus of IBV-infected cells (Table II). In the nucleolar proteome, 12 proteins (2.4%) showed ≥2.0-fold reduction in the nucleolus of IBV-infected cells, and 22 proteins (4.5%) showed ≥2.0-fold increase in the nucleolus of IBV-infected cells (Table III).

*Bioinformatic Analyses of Vero Cell Proteome*—Data sets of the total number of proteins identified from the cytoplasmic, nuclear, and nucleolar fractions were uploaded to Ingenuity Pathway Analysis, which then assigned identified proteins into different molecular and cellular functional classes (see supplemental Table 4 for definitions) based on underlying biological evidence from the literature database. The relative proportion of proteins in each separate functional class is shown as a series of pie charts (Fig. 3), and the data indicated that the proteome differed between the cytoplasm, nucleus, and nucleolus. For example, the relative proportion of proteins involved in RNA post-transcriptional modification and gene expression was greater in the nuclear and nucleolar proteomes than in the cytoplasmic proteome, whereas in the cytoplasmic proteome, the relative proportion of proteins involved in protein degradation was greater than in the nuclear or nucleolar proteome.

*Network Pathway Analysis Predicted Novel Interactions with Cellular Signaling Cascades*—Ingenuity Pathway Analysis was used to determine whether proteins that changed in abundance could be mapped to specific functional networks. For the cytoplasmic and nuclear proteomes, network analysis suggested that proteins involved in cellular assembly, organization, morphology, signaling, and growth changed in abundance in IBV-infected cells (Figs. 4 and 5 for the cytoplasmic and nuclear proteomes, respectively). Many of these proteins were linked to the NF-κB and AP-1 signaling cascades as were proteins associated with the nucleolar proteome (Fig. 6). Although the response of NF-κB to various SARS-CoV proteins was evaluated in several overexpression systems expressing different virus proteins, there were differing results (42–44). The response of AP-1 in coronavirus-infected cells or NF-κB in IBV-infected cells has not been determined previously. AP-1 is a transcription factor composed of dimeric basic region-leucine zipper proteins that belong to the Jun, Fos, Maf, and activating transcription factor subfamilies (45). Similar to NF-κB, AP-1 regulates a wide range of cellular processes, including differentiation, proliferation, survival, and death (45). Specific proteins up-regulated in IBV-infected cells and known to be associated with the AP-1 network included HSPB1 (heat shock protein 27-kDa protein 1, HSP27), whose transcription is dependent on NF-κB (46) and in turn can increase activation of Erk1/2 (47) and p38 mitogen-activated protein kinase (MAPK) cascades (48). NF-κB is a protein complex, which among other proteins is composed of RelA and p50. These proteins can traffic to the nucleus to activate NF-κB-responsive genes.

TABLE II

*Nuclear proteins identified by LC-MS/MS demonstrating ≥2-fold change in abundance in response to IBV infection*

Notes on protein function were obtained from annotations in the UniProt database. G6P, glucose-6-phosphate; LDH, lactate dehydrogenase; pol, polymerase; PG, phosphoglycerate.

| Protein ID | Name | Ratio | Peptides | Sequence coverage | FPR | Function |
|---|---|---|---|---|---|---|
| | | | | % | | |
| Proteins present in increased abundance in IBV-infected cells | | | | | | |
| IPI00816452 | Myosin VI | 90.4 | 7 | 1.2 | 0.010476 | Motor protein, p53-responsive, enhances RNA pol II transcription |
| IPI00646779 | Tubulin β-6 chain | 10.8 | 5 | 8.7 | $1.21 \times 10^{-41}$ | Major constituent of microtubules |
| IPI00171438 | TXNDC5 | 3.9 | 2 | 6 | 0.001762 | Thioredoxin activity |
| IPI00658097 | HMGN1 | 2.8 | 5 | 18.1 | $2.60 \times 10^{-14}$ | Nucleosome binding |
| IPI00293845 | RIF1 | 2.0 | 2 | 0.4 | 0.003549 | Cell cycle, peak expression in late $G_2$/S phase |
| Proteins present in decreased abundance in IBV-infected cells | | | | | | |
| IPI00414676 | HSP90-β | 2.0 | 6 | 11.5 | $4.66 \times 10^{-72}$ | Chaperone, stress response |
| IPI00219757 | GSTP1-1 | 2.0 | 1 | 18.1 | 0.004648 | Antiapoptotic, glutathione conjugation |
| IPI00295386 | CBR1 | 2.0 | 3 | 6.1 | $2.29 \times 10^{-23}$ | Catalyzes the reduction of a range of carbonyl compounds |
| IPI00184848 | ABCB11 | 2.0 | 1 | 1.3 | $2.58 \times 10^{-61}$ | ATP-dependent export of bile salts and sodium |
| IPI00479186 | PKM2 | 2.0 | 9 | 17.9 | $7.24 \times 10^{-97}$ | ATP generation |
| IPI00887678 | LOC654188 | 2.0 | 6 | 13 | $2.23 \times 10^{-10}$ | Peptidyl-prolyl isomerase activity |
| IPI00376344 | Myosin Ib | 2.0 | 5 | 6.4 | $6.81 \times 10^{-76}$ | Motor protein, cell migration and vesicular transport |
| IPI00375531 | NDK A | 2.0 | 3 | 7.9 | $1.73 \times 10^{-6}$ | Nucleoside triphosphate synthesis, cell cycle |
| IPI00843975 | Ezrin | 2.0 | 6 | 15 | $9.31 \times 10^{-71}$ | A determinant of cell shape |
| IPI00333770 | Zizimin-3 | 2.0 | 2 | 0.6 | $1.04 \times 10^{-5}$ | Potential guanine nucleotide exchange factor |
| IPI00554481 | 4F2hc | 2.0 | 7 | 8.9 | $1.16 \times 10^{-93}$ | Animo acid transport, required for cell growth |
| IPI00747849 | ATP1B1 | 2.1 | 2 | 4.6 | 0.001511 | Ion transport |
| IPI00105407 | AKR1B10 | 2.1 | 2 | 12 | $4.27 \times 10^{-24}$ | Acts as all-*trans*-retinaldehyde reductase |
| IPI00413641 | Aldose reductase | 2.1 | 2 | 5.7 | 0.000461 | NADPH-dependent reduction of carbonyl-containing compounds |
| IPI00219675 | p21-Rac1 | 2.1 | 3 | 13.3 | 0.005477 | Small GTPase; roles in cell polarization, cell migration |
| IPI00910781 | G6P isomerase | 2.2 | 5 | 4.6 | $4.60 \times 10^{-32}$ | Carbohydrate degradation |
| IPI00219365 | Moesin | 2.2 | 3 | 12.8 | $5.74 \times 10^{-59}$ | Plasma membrane structure |
| IPI00910979 | Pyruvate kinase | 2.3 | 2 | 22.1 | $1.44 \times 10^{-164}$ | Pyruvate kinase |
| IPI00219217 | LDH B-chain | 2.3 | 3 | 9.9 | $3.67 \times 10^{-16}$ | L-Lactate dehydrogenase activity |
| IPI00297477 | U2 snRNP A | 2.3 | 2 | 9.4 | 0.003467 | mRNA splicing via the spliceosome |
| IPI00465248 | α-Enolase | 2.4 | 9 | 27.9 | $8.17 \times 10^{-102}$ | Glycolysis, growth control, hypoxia tolerance |
| IPI00216298 | Thioredoxin | 2.4 | 2 | 10.5 | 0.004965 | Participates in redox reactions, cell motion, and proliferation |
| IPI00218914 | Retinal dehydrogenase 1 | 2.5 | 12 | 20 | $1.44 \times 10^{-12}$ | Cofactor and retinol metabolism |
| IPI00010896 | CLIC1 | 2.5 | 3 | 15.8 | $1.28 \times 10^{-10}$ | Chloride ion channel activity, pH-dependent |
| IPI00003269 | κ-Actin | 2.5 | 1 | 19.1 | $5.94 \times 10^{-47}$ | Cell motility, cytoskeleton |
| IPI00453476 | PG mutase | 2.5 | 6 | 12.6 | $1.56 \times 10^{-12}$ | Glycolysis, phosphoglycerate mutase |
| IPI00169383 | Phosphoglycerate kinase 1 | 2.6 | 4 | 5.8 | 0.00015 | Glycolysis, primer recognition protein |
| IPI00032826 | Hsc70-interacting protein | 2.6 | 6 | 3.5 | 0.005148 | Chaperone |
| IPI00795918 | NCAM-1 | 2.7 | 6 | 5.2 | 0.002325 | Cell adhesion |
| IPI00643920 | Transketolase | 2.8 | 4 | 5.5 | $4.12 \times 10^{-15}$ | Connects the pentose phosphate pathway to glycolysis |
| IPI00299024 | BSAP1 | 2.9 | 2 | 35.2 | $2.38 \times 10^{-43}$ | Cell growth/projection |
| IPI00219301 | MARCKS | 2.9 | 1 | 4.5 | 0.000205 | Cytoskeleton, actin binding |
| IPI00219219 | Galectin-1 | 3.1 | 1 | 34.8 | $8.32 \times 10^{-63}$ | Apoptosis, cell differentiation, cell proliferation |
| IPI00216691 | Profilin-1 | 3.2 | 2 | 34.3 | $1.09 \times 10^{-8}$ | Modulates actin polymerization |
| IPI00217466 | Histone H1c | 4.5 | 1 | 19.5 | $8.35 \times 10^{-100}$ | Nucleosome formation and structure |

*Validation of Signaling Pathway Activation in IBV-infected Cells*—To validate the network pathway analysis and determine whether AP-1 and/or NF-κB was up-regulated in IBV-infected cells, a reporter gene system was used in which expression of the reporter protein luciferase was under the control of promoter(s) recognized by either the AP-1 or NF-κB transcription complex. As a positive control, Sendai virus, which has been shown previously to stimulate signaling cas-

TABLE III

*Nucleolar proteins identified by LC-MS/MS demonstrating ≥2-fold change in abundance in response to IBV infection*

Notes on protein function were obtained from annotations in the UniProt database. snRNP, small nuclear ribonucleoprotein; COX, cytochrome *c* oxidase; NPC, nuclear pore complex; PDI, protein-disulfide isomerase.

| Protein ID | Name | Ratio | Peptides | Sequence coverage | FPR | Function |
|---|---|---|---|---|---|---|
| | | | | % | | |
| Proteins present in increased abundance in IBV-infected cells | | | | | | |
| IPI00019590 | tPA | 7.8 | 2 | 4.8 | $1.15 \times 10^{-13}$ | Tissue remodeling, degradation, cell migration |
| IPI00328840 | Aly | 6.5 | 1 | 4.2 | $7.76 \times 10^{-7}$ | mRNA splicing and export |
| IPI00012066 | PCBP2 | 3.0 | 1 | 5.5 | $2.76 \times 10^{-10}$ | RNA binding |
| IPI00741608 | eIF 5A-1 | 2.7 | 2 | 8.4 | $1.94 \times 10^{-14}$ | Protein biosynthesis |
| IPI00853009 | CELF-1 | 2.6 | 2 | 5.5 | $2.67 \times 10^{-6}$ | Alternative splicing, mRNA translation and stability |
| IPI00023860 | NAP1L1 | 2.5 | 4 | 13.8 | $1.02 \times 10^{-9}$ | Modulation of chromatin formation and regulation of cell proliferation |
| IPI00298994 | Talin-1 | 2.5 | 3 | 1.9 | 0.000312 | Cytoskeleton anchoring at plasma membrane |
| IPI00028122 | PSIP1 | 2.5 | 2 | 4.9 | $2.44 \times 10^{-6}$ | Cell differentiation and stress responses |
| IPI00290204 | U1 snRNP 70 kDa | 2.4 | 1 | 3.7 | 0.000982 | RNA splicing |
| IPI00744851 | DSP | 2.3 | 1 | 7.1 | 0.001515 | Cytoskeleton |
| IPI00007818 | CPSF3 | 2.3 | 2 | 4.2 | $5.31 \times 10^{-6}$ | mRNA processing |
| IPI00031627 | RPB1 | 2.3 | 2 | 1.2 | $8.39 \times 10^{-8}$ | Transcription |
| IPI00011654 | Tubulin $\beta$ chain | 2.2 | 5 | 17.6 | $2.37 \times 10^{-22}$ | Major constituent of microtubules |
| IPI00477040 | NUP188 | 2.2 | 2 | 1.8 | $6.37 \times 10^{-6}$ | May function as part of the nuclear pore complex |
| IPI00030275 | HSP75 | 2.1 | 3 | 4.3 | $1.23 \times 10^{-11}$ | Chaperone |
| IPI00003377 | SFRS7 | 2.1 | 4 | 20.6 | $1.26 \times 10^{-23}$ | Pre-mRNA splicing, can modulate alternative splicing *in vitro* |
| IPI00011698 | SAP18 | 2.1 | 2 | 22.2 | $4.86 \times 10^{-14}$ | Transcriptional repression. |
| IPI00646899 | RPL10 | 2.1 | 1 | 6.1 | $4.72 \times 10^{-8}$ | Ribosome constituent |
| IPI00221222 | PC4 | 2.0 | 1 | 10.2 | $7.45 \times 10^{-8}$ | Transcriptional regulation |
| IPI00555744 | RPL14 | 2.0 | 1 | 5.5 | $9.09 \times 10^{-44}$ | RNA binding, ribosomal protein |
| IPI00163505 | RBM39 | 2.0 | 1 | 2.8 | $7.78 \times 10^{-17}$ | Transcriptional coactivator, mRNA processing/splicing |
| IPI00397904 | NUP93 | 2.0 | 2 | 3.3 | $8.64 \times 10^{-11}$ | Part of the nuclear pore complex, required for correct NPC assembly |
| IPI00217357 | CARP-1 | 2.0 | 3 | 3.7 | $5.20 \times 10^{-5}$ | Cell cycle regulation, cell proliferation, and potential apoptosis signaling |
| Proteins present in decreased abundance in IBV-infected cells | | | | | | |
| IPI00294744 | PARN | 2.0 | 5 | 9.7 | $9.65 \times 10^{-17}$ | Nonsense-mediated mRNA decay, 3′ poly(A) tail degradation |
| IPI00220362 | HSP10 | 2.0 | 3 | 33.3 | $2.07 \times 10^{-10}$ | Stress response |
| IPI00010796 | PDI | 2.1 | 7 | 16.3 | $1.14 \times 10^{-47}$ | Chaperone, disulfide bond creation, rearrangement, and dissolution |
| IPI00054042 | GTFII-I | 2.2 | 3 | 2.9 | 0.001192 | Transcription, coordinates complex formation at the c-FOS promoter |
| IPI00024662 | CBX5 | 2.2 | 1 | 6.8 | $1.19 \times 10^{-5}$ | Chromatin binding, transcriptional repression |
| IPI00178440 | EF-1$\beta$ | 2.3 | 1 | 6.7 | $2.73 \times 10^{-11}$ | Translation elongation activity |
| IPI00328987 | Bystin | 2.3 | 1 | 3.4 | 0.001063 | Cell adhesion, ribosome biogenesis |
| IPI00182540 | Catenin $\delta$1 | 2.3 | 1 | 1.5 | $4.90 \times 10^{-5}$ | Cell adhesion, transcription, transcriptional regulation |
| IPI00024911 | ERp29 precursor | 2.4 | 2 | 9.6 | $2.90 \times 10^{-18}$ | Chaperone |
| IPI00006579 | COX IV-1 | 2.8 | 2 | 14.8 | 0.001749 | Cytochrome *c* oxidase activity |
| IPI00383815 | GFAP | 3.1 | 4 | 8.2 | $1.26 \times 10^{-19}$ | Class III intermediate filament |
| IPI00062120 | S100A16 | 3.4 | 2 | 15.5 | $1.05 \times 10^{-13}$ | Calcium-binding nucleolar protein |

cades, was used to infect cells (Fig. 7*A*). The data indicated that luciferase activity was ~2.5-fold higher in IBV-infected cells compared with mock-infected cells and therefore suggested that AP-1-driven transcription increased as a result of virus infection (Fig. 7*A*). Two independent systems were used to measure intracellular NF-κB p50/RelA heterodimer activity. The NF-κB promoter, which is synthetic, has three NF-κB (concanavalin A)-dependent elements and the PRDII promoter, and which occurs in native systems, is activated by NF-κB to produce interferon β. Both reporter systems give rise to expression of a luciferase gene, allowing the relative amount of luciferase present to be analyzed, reflecting promoter activity and hence NF-κB activation. Cells were either mock-infected or infected with IBV and transfected with the appropriate reporter gene constructs. The data indicated that for both reporter gene systems the level of luciferase in IBV-

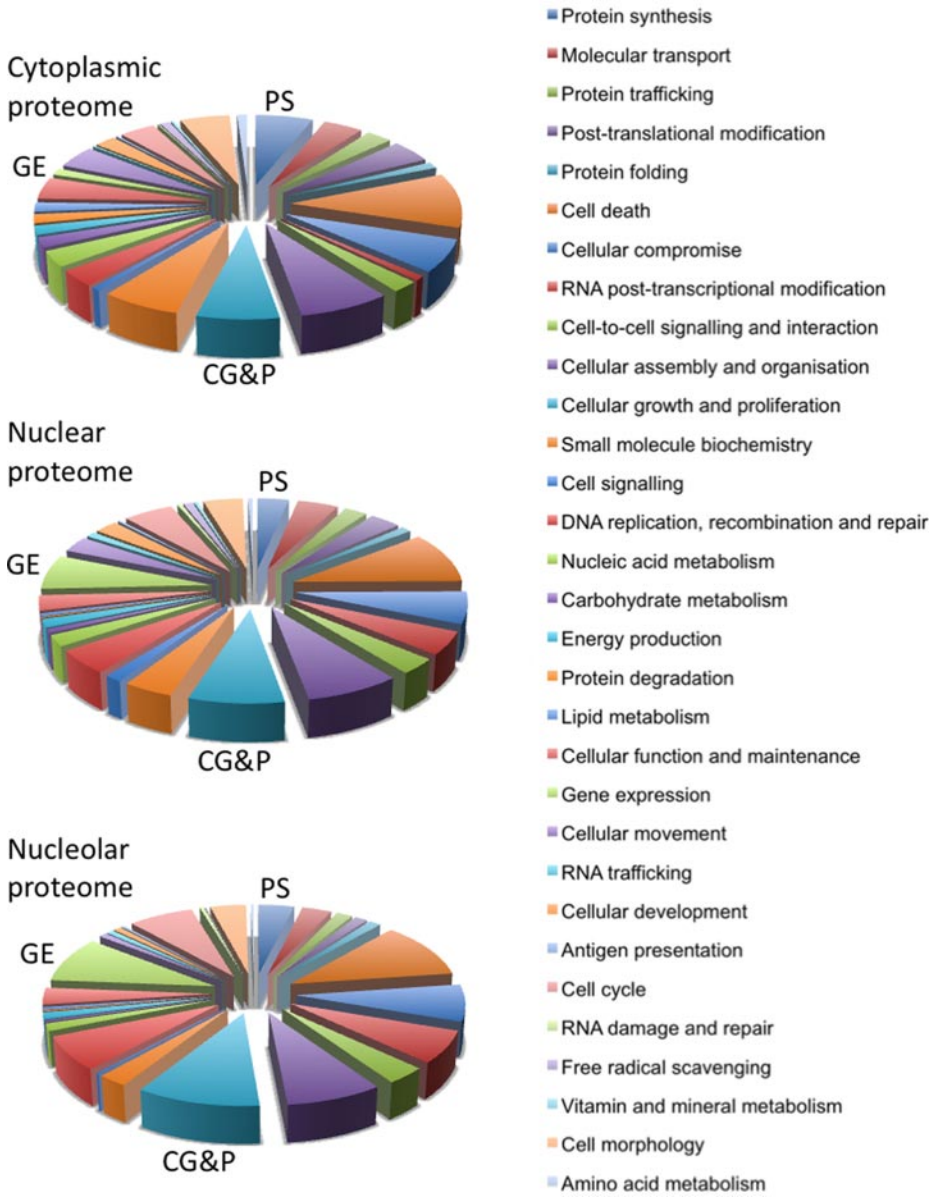


FIG. 3. **Analysis of relative proportion of different protein groups and functional classes (indicated in legend) in nuclear, cytoplasmic, and nucleolar proteomes of Vero cells.** For orientation, the first grouping, protein synthesis, is to the *right* of the *12 o'clock position*. Protein synthesis, cellular growth and proliferation, and gene expression are indicated as *PS*, *CG&P*, and *GE*, respectively.

infected cells was greater than in mock-infected cells. There was an ~6- and 4-fold increase in luciferase activity in IBV-infected cells with reporter gene using the PRDII- or concanavalin A promoter-based assay, respectively (Fig. 7*A*).

As an independent validation, we predicted that if the canonical pathway was initiated upon infection with IBV NF-κB p50/RelA will be activated and there will be a redistribution of the p50/RelA heterodimer from cytoplasm to nucleus within the cell. To distinguish this, cells were infected with IBV, and indirect immunofluorescence confocal microscopy was used to determine the localization of p50 and RelA in mock- and IBV-infected cells (Fig. 7*B*). The data indicated that in mock-infected cells p50 and RelA were distributed throughout the cytoplasm and nucleus. In contrast, in IBV-infected cells, the localization of p50 and RelA was predominantly nuclear.

*Cellular Scaffolding and Trafficking Proteins Were Redistributed in IBV-infected Cells*—The quantitative proteomics analysis revealed that several different cellular proteins involved in cell morphology and the cytoskeleton changed in abundance in IBV-infected cells. For example, MYO6, a protein involved in endocytic vesicle trafficking (49) and cargo transport (50), was enriched in the nuclear proteome (90-fold increase; Table I) in IBV-infected cells. Vimentin is a major component of type III intermediate filaments and was increased in abundance in the cytoplasmic proteome of IBV-infected cells (Table II). The subcellular localization of these two proteins was investigated in IBV-infected cells and compared with mock-infected cells using indirect immunofluorescence confocal microscopy. The data indicated that in mock-infected cells the subcellular localization of MYO6 was predominately cytoplasmic (Fig. 8*A*),

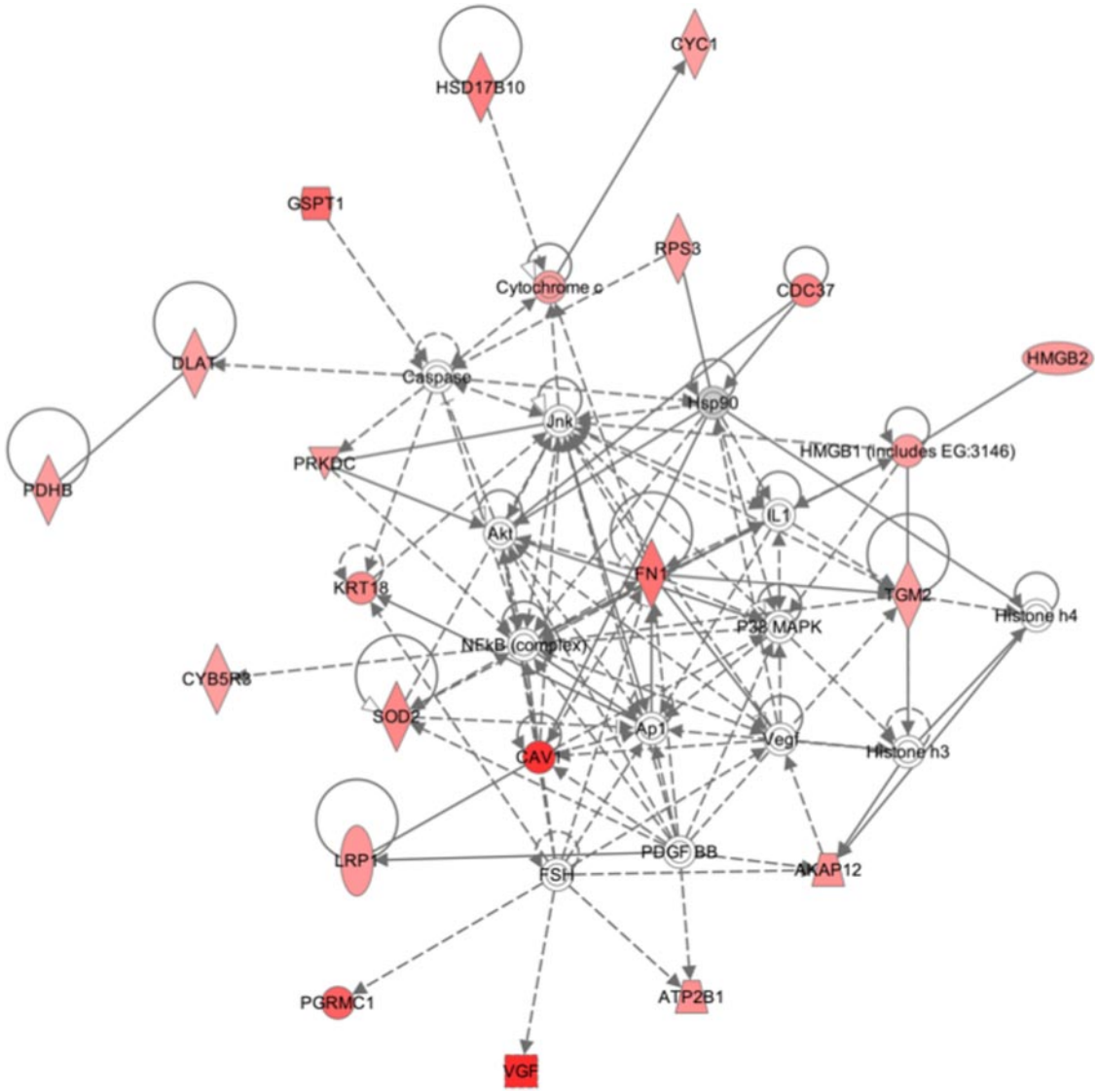


FIG. 4. **Ingenuity Pathway Analysis of proteins predominately associated with assembly and organization in nuclear proteome.** Proteins shaded in *green* indicate 2-fold or more depleted in IBV-infected cells, and proteins shaded in *red* indicate 2-fold or more increased in the nuclear proteome. Proteins in *gray* were identified in the analysis but did not meet the 2-fold specified cutoff value between mock- and IBV-infected cells. Proteins in *white* are those identified from the Ingenuity Pathways Knowledge Base. The *shapes* are indicative of the molecular class (*i.e.* protein family) (see supplemental Fig. 2 for the legend). *Lines* connecting the molecules indicate molecular relationships. There are two line styles; *dashed lines* indicate indirect interactions, and *solid lines* indicate direct interactions. The style of the *arrows* indicates specific molecular relationships and the directionality of the interaction (A acts on B).

whereas in IBV-infected cells, MYO6 also exhibited perinuclear and nuclear punctate staining (Fig. 8*A*), which verified the increased nuclear abundance of MYO6 determined by the SILAC analysis (Table I). In IBV-infected cells, the abundance and distribution of vimentin were different from those in mock-infected cells. In mock-infected cells, vimentin was distributed in the cytoplasm with enrichment in the perinuclear region (Fig. 8*B*), whereas in IBV-infected cells that form syncytia, this enrichment was lost (Fig. 8*B*), again validating the change in the amount of vimentin determined by the SILAC analysis (Table II). β-Tubulin was identified as being 2.2-fold increased in the nucleolar fraction from IBV-infected cells by SILAC analysis (Table III). This again was validated by the observed increase of β-tubulin in nucleolar fractions from IBV-infected cells by Western blot (Fig. 1*D*).

*Changes in Nucleolar Proteome in Response to Virus Infection Are Not Conserved*—The interaction of virus infection with the nucleolus has been predicted to alter the nucleolar proteome (23, 25, 51). This hypothesis was investigated in a recent quantitative proteomics analysis using SILAC coupled to LC-MS/MS that revealed only specific nucleolar proteins changed in abundance in response to adenovirus (a double-stranded DNA virus that replicates in the nucleus) infection rather than total global changes (52). A similar observation

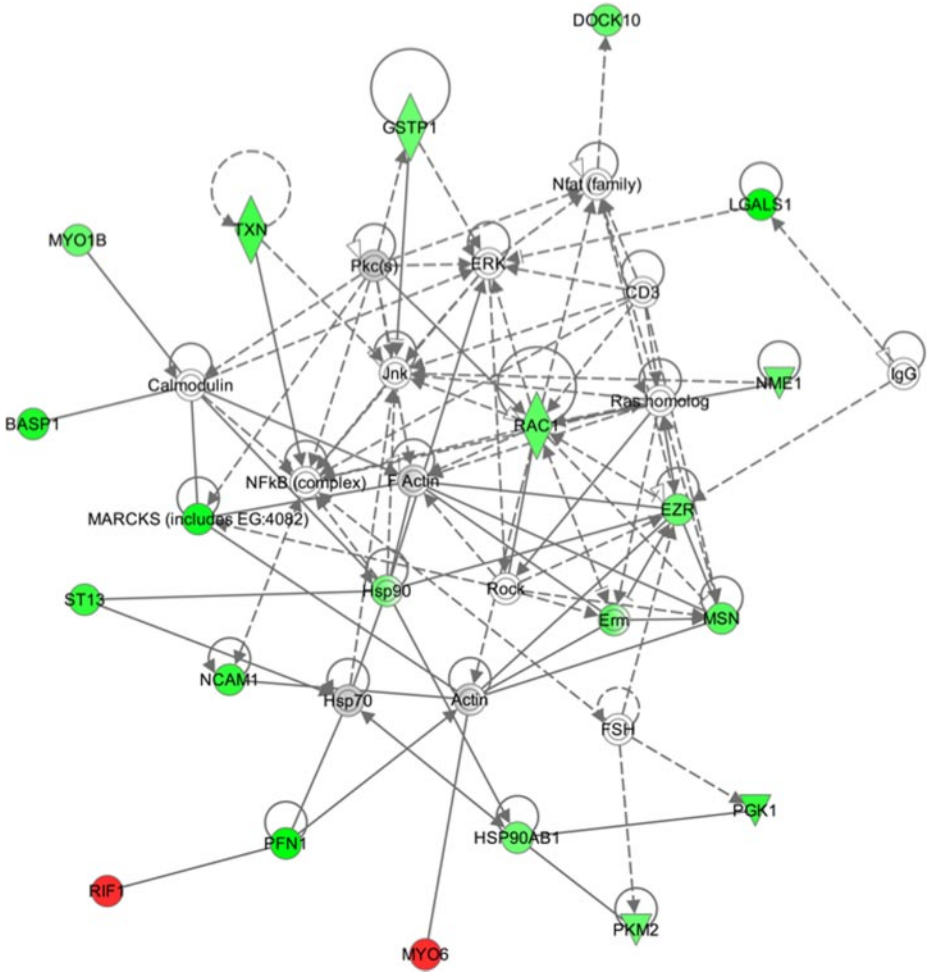


FIG. 5. **Ingenuity Pathway Analysis of proteins predominately associated with cellular assembly and organization in cytoplasmic proteome.** Proteins shaded in *green* indicate 2-fold or more depleted in IBV-infected cells, and proteins shaded in *red* indicate 2-fold or more increased in the nuclear proteome. Proteins in *gray* were identified in the analysis but did not meet the 2-fold specified cutoff value between mock- and IBV-infected cells. Proteins in *white* are those identified from the Ingenuity Pathways Knowledge Base. The *shapes* are indicative of the molecular class (*i.e.* protein family) (see supplemental Fig. 2 for the legend). *Lines* connecting the molecules indicate molecular relationships. There are two line styles; *dashed lines* indicate indirect interactions, and *solid lines* indicate direct interactions. The style of the *arrows* indicates specific molecular relationships and the directionality of the interaction (A acts on B).

was found in this study in that the abundance of only specific nucleolar proteins changed in response to IBV infection. Comparison of the amounts of proteins that were common to both data sets indicated that not all of the same proteins were altered in virus-infected cells (Fig. 9).

## DISCUSSION

Virus infection has multiple effects on host cell processes, such as signaling pathways and morphology. High throughput quantitative proteomics using SILAC is an ideal methodology to map such changes from the perspective of a total cell as it is suited to unbiased comparison analysis (39), *e.g.* virus-infected *versus* uninfected cells. Previously, to our knowledge, SILAC analysis has only been applied to the interaction of three viruses with the host cell, hepatitis C virus (53), pseudorabies virus (PrV) (40), and adenovirus. Hepatitis C virus is a positive strand RNA virus, and SILAC was used to investigate its interaction with host cell lipid rafts. In this study, 1036 proteins were identified by SILAC with LC-MS/MS compared with 100 proteins identified by two-dimensional gel electrophoresis (53). PrV I-like adenovirus is a double-stranded DNA virus that replicates in the nucleus. For PrV I, SILAC was used in conjunction with two-dimensional gel electrophoresis and phosphoprotein enrichment to identify 2600 proteins representing 565 genes. Changes were identified in proteins associated with intracellular transport and trafficking as well as HSP27 (40). For adenovirus infection, SILAC was applied to study changes in the nucleolar proteome in response to infection. More frequently, two-dimensional gel electrophoresis has been used to investigate the interaction of a number of different RNA viruses that replicate in the cytoplasm with subcellular compartments and/or the host cell. For example, 24 different proteins were identified as changing in the nuclear proteome of respiratory syncytial virus-infected cells (54). These included components of the cytoskeleton, RNA helicases, and heat shock proteins (54). Analysis of infectious bursal disease virus-infected cells identified 51 altered cellular proteins, including cytoskeletal proteins, ribosomal proteins, translation factors, and heat shock proteins (55). Analysis of dengue virus-infected cells identified changes in 17 differentially expressed proteins (56).

In this study of Vero cells infected with IBV, a total of 1830 cellular and two viral proteins was identified and quantified. Vero cell lines are commonly used in studying virus-host cell

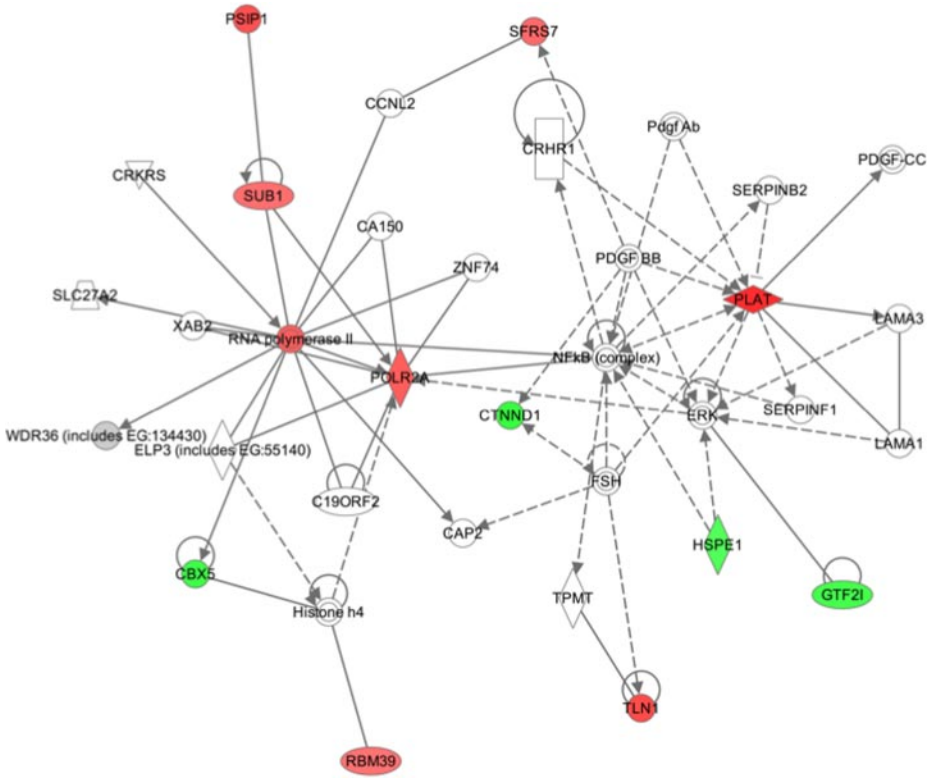


FIG. 6. **Ingenuity Pathway Analysis of proteins predominately associated with cell growth and interaction in nucleolar proteome.** Proteins shaded in *green* indicate 2-fold or more depleted in IBV-infected cells, and proteins shaded in *red* indicate 2-fold or more increased in the nuclear proteome. Proteins in *gray* were identified in the analysis but did not meet the 2-fold specified cutoff value between mock- and IBV-infected cells. Proteins in *white* are those identified from the Ingenuity Pathways Knowledge Base. The *shapes* are indicative or the molecular class (*i.e.* protein family) (see supplemental Fig. 2 for the legend). *Lines* connecting the molecules indicate molecular relationships. There are two line styles; *dashed lines* indicate indirect interactions, and *solid lines* indicate direct interactions. The style of the *arrows* indicates specific molecular relationships and the directionality of the interaction (A acts on B).

interactions as it is permissive to infection by many different viruses. The viral N protein was present in all three samples and validated previous overexpression and infection experiments where N protein, which contains appropriate trafficking signals (57, 58), was shown to be predominately localized to the cytoplasm but also to the nucleus and nucleolus (59–61). M protein was identified in the cytoplasmic proteome from IBV-infected cells but not in the nuclear or nucleolar proteome. This protein has been shown previously to localize to the Golgi region in IBV-infected cells (62, 63) and therefore also provides an internal control for the purity of the different extracts. No other viral proteins were detected. However, compared with the N and the M proteins, these proteins are less abundant and might therefore have been below the threshold level of detection.

SILAC coupled to LC-MS/MS differentiated changes in the host cell in response to infection with IBV. These were investigated using techniques independent of subcellular fractionation, including functional assays on replicate samples and indirect immunofluorescence confocal microscopy of selected proteins. Network pathway analysis indicated that in the proteomes examined cellular proteins could be linked to signaling cascades such as NF-κB, MAPK, and ERK. The interaction of IBV with these pathways has not been described previously and in general in coronaviruses has only been examined in the context of overexpression of specific viral proteins rather than in virus-infected cells. For example, overexpression of different SARS-CoV proteins has been reported to have differing effects, either activation or inhibition on NF-κB activity (42, 43, 64). AP-1 has been shown to be induced in cells overexpressing the SARS-CoV spike glycoprotein (65) and N protein (66). From the pathway analysis, we predicted that AP-1 and NF-κB signaling would be activated in IBV-infected cells. This was examined using a reporter gene-based system in which the presence of AP-1 and NF-κB activates the transcription (and subsequent expression) of luciferase. The data indicated that AP-1 was activated 2.5-fold in IBV-infected cells, similar to that reported in the overexpression studies of SARS-CoV proteins (65, 66). AP-1 proteins have important effects on cellular proliferation (67), and activation of proteins within this pathway could account for observed ablation of D-type cyclins in IBV-infected cells (1, 68). Likewise, this is the first description of the activation of NF-κB in IBV-infected cells and together with the independent observations that p50 and RelA traffic to the nucleus in IBV-infected cells confirms that coronaviruses can activate this pathway. These observations were a direct and independent validation of the bioinformatics analysis of the quantitative proteomics data.

One of the major findings was that the abundance and distribution of proteins involved in maintenance of cellular structure were altered in IBV-infected cells. This confirms previous observations that have shown rearrangement of Golgi apparatus (69) and microtubules (70) or highlighted the role of actin in assembly and budding (71) in coronavirus-infected cells. Two proteins specifically validated using immu-

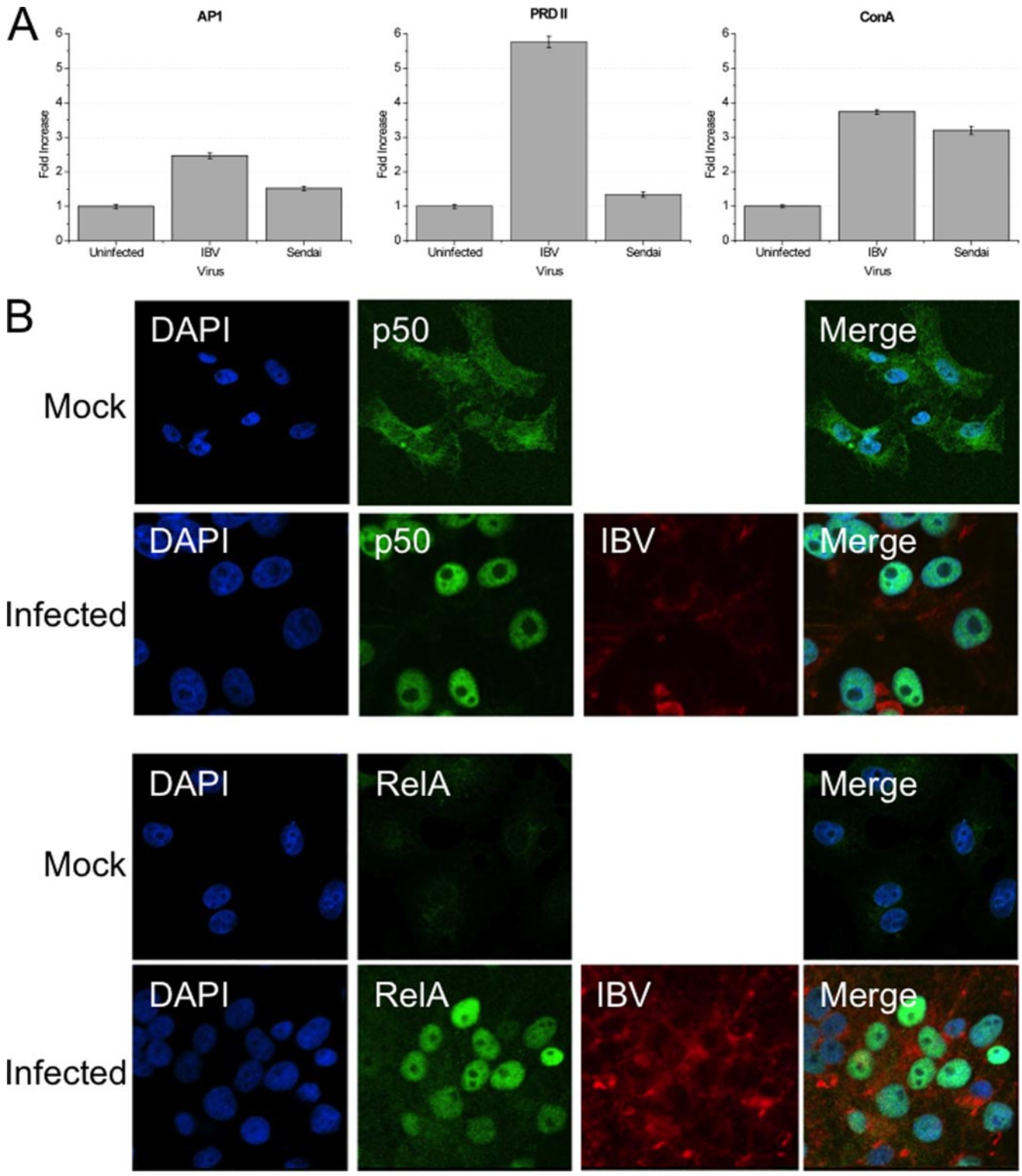


FIG. 7. *A*, histogram of the luciferase reporter gene assays to assess the relative level of AP-1- and NF-κB-driven transcription in mock-, Sendai virus-, and IBV-infected cells. Data are an average of 12 independent experiments. *B*, indirect immunofluorescence confocal microscopy analysis of the localization of either p50 or RelA (both *green*) in either mock- or IBV-infected (*red*) cells. Nuclei are stained with DAPI, and a merged image is also presented. *ConA*, concanavalin A.

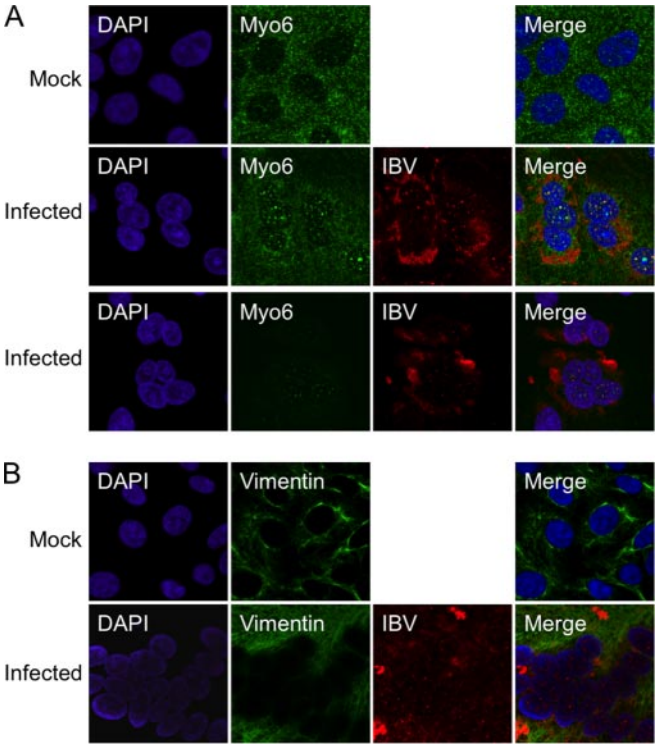


FIG. 8. **Indirect immunofluorescence analysis using confocal microscopy of MYO6 (*A*) or vimentin (*B*) in mock- or IBV-infected cells.** MYO6 and vimentin are shown in *green*, nuclei are stained with DAPI (*blue*), and IBV proteins are shown in *red*. A merged image is also presented. For *A*, two examples of IBV-infected cells are shown: *top*, the MYO6 cytoplasmic signal is in the same linear range as the MYO6 signal in the mock-infected cells; *bottom*, the MYO6 signal in the nucleus is in the linear range. Note that the IBV-infected cells identified in *B* are an example of virus-induced syncytia.

nofluorescence were MYO6 and vimentin, neither of which has been identified previously as being altered in coronavirus-infected cells. MYO6 showed enhanced punctate nuclear staining and staining of the perinuclear region in IBV-infected cells reminiscent of the distribution of MYO6 in cells treated with $\alpha$-amanitin, an inhibitor of RNA polymerase II (72). This pattern of redistribution has been described for MYO6 as a p53-induced stress response (73). In IBV-infected cells, vimentin accumulated in the cytoplasm in virus-induced syncytia. Vimentin has been shown previously to be disrupted in the RNA viruses, infectious bursal disease virus (55), bluetongue virus (74), and dengue virus-infected cells (75), and in the DNA viruses, African swine virus (76) and vaccinia virus-infected cells (77). In many of these cases, vimentin has been suggested to have a role in virus assembly and egress.

Analysis of the nucleolar proteome identified and quantified 506 proteins, a proportion of which showed either increased or decreased abundance in virus-infected cells. This validates the hypotheses that the nucleolar proteome can be altered in RNA virus-infected cells (23). The data indicated that in IBV-infected cells there was no significant difference in the abundance of the proteins that are responsible for the formation of the nucleolus (78), such as nucleolin, nucleophosmin, and fibrillarin, potentially indicating that proteome changes as a result of virus infection are to specific proteins rather than generic to the nucleolus. This reflected the findings of a quantitative proteomics analysis of the nucleolus in cells infected with adenovirus (52). Other viruses, such as the DNA virus herpes simplex virus type 1, which replicates in the nucleus and some of whose proteins localize to the nucleolus (79, 80), can induce the redistribution of nucleolin and fibrillarin in virus-infected cells (81, 82). Similarly, adenovirus infection resulted in the redistribution of nucleolin and nucleophosmin (83). However, how these alterations may affect nucleolar

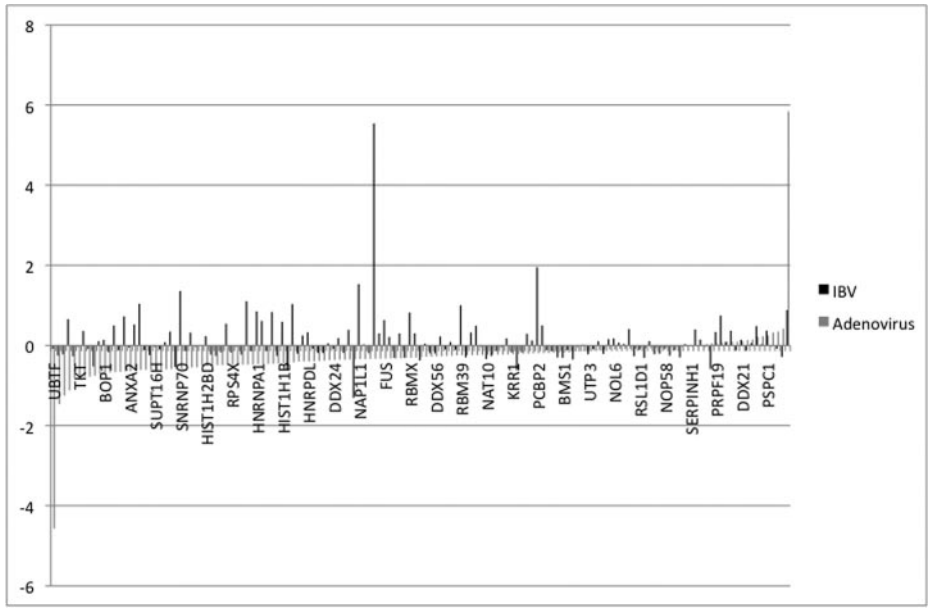


FIG. 9. **Comparison of relative abundance of proteins identified in nucleolus in cells infected with either IBV (*black*) or adenovirus (*gray*).** Selected gene names are used as identifiers.

function is not known. Interestingly, upstream binding factor can be recruited to adenovirus DNA replication centers without an apparent ablation in rRNA synthesis or alteration in the localization of RNA polymerase I (84). In IBV-infected cells, proteins associated with RNA post-transcriptional modifications, such as splicing, cleavage of mRNA, and processing of mRNA, showed differential abundance in the nucleolus. Changes in the abundance of such proteins may account for the regulation of specific host cell mRNAs observed in coronavirus-infected cells (85).

Similar to that observed in a quantitative analysis of PrV-infected cells (40), the majority of the cellular proteome remained relatively unchanged in IBV-infected cells, suggesting that specific changes occur in response to virus infection. High throughput quantitative proteomics using SILAC is an ideal methodology to study the cellular proteome during virus infection. The use of multiple isotope labeling lends itself to the simultaneous analysis of different strains of the same virus that show different pathogenic phenotypes to determine whether changes in the cellular proteome can be correlated with infectivity.

*Acknowledgments*—Prof. Tom Wileman at the University of East Anglia is thanked for the gift of the anti-vimentin antibody. Dr. David A. Matthews at the University of Bristol is thanked for provision of adenovirus nucleolar data sets.

* This work was supported in part by a Leverhulme fellowship (to J. A. H.).

S This article contains supplemental Figs. 1 and 2 and Tables 1–4.

¶ Supported by a Biotechnology and Biological Sciences Research Council (BBSRC) doctoral training grant awarded to the Astbury Centre for Structural Molecular Biology, University of Leeds, UK.

‖Supported by a BBSRC project grant (to J. A. H.).

‡‡ To whom correspondence should be addressed: Inst. of Molecular and Cellular Biology, Garstang Bldg., Rm. 8.58, Faculty of Biological Sciences, University of Leeds, Leeds LS2 9JT, UK. E-mail: j.a.hiscox@leeds.ac.uk.

REFERENCES

1. Dove, B., Brooks, G., Bicknell, K., Wurm, T., and Hiscox, J. A. (2006) Cell cycle perturbations induced by infection with the coronavirus infectious bronchitis virus and their effect on virus replication. *J. Virol.* **80,** 4147–4156
2. Chen, C. J., and Makino, S. (2004) Murine coronavirus replication induces cell cycle arrest in G0/G1 phase. *J. Virol.* **78,** 5658–5669
3. Chen, C. J., Sugiyama, K., Kubo, H., Huang, C., and Makino, S. (2004) Murine coronavirus nonstructural protein p28 arrests cell cycle in G0/G1 phase. *J. Virol.* **78,** 10410–10419
4. Li, F. Q., Tam, J. P., and Liu, D. X. (2007) Cell cycle arrest and apoptosis induced by the coronavirus infectious bronchitis virus in the absence of p53. *Virology* **365,** 435–445
5. Belyavsky, M., Belyavskaya, E., Levy, G. A., and Leibowitz, J. L. (1998) Coronavirus MHV-3-induced apoptosis in macrophages. *Virology* **250,** 41–49
6. Eleouet, J. F., Chilmonczyk, S., Besnardeau, L., and Laude, H. (1998) Transmissible gastroenteritis coronavirus induces programmed cell death in infected cells through a caspase-dependent pathway. *J. Virol.* **72,** 4918–4924
7. Versteeg, G. A., Slobodskaya, O., and Spaan, W. J. (2006) Transcriptional profiling of acute cytopathic murine hepatitis virus infection in fibroblast-like cells. *J. Gen. Virol.* **87,** 1961–1975
8. Whitman, L., Zhou, H., Perlman, S., and Lane, T. E. (2009) IFN-gamma-mediated suppression of coronavirus replication in glial-committed progenitor cells. *Virology* **384,** 209–215
9. Tohya, Y., Narayanan, K., Kamitani, W., Huang, C., Lokugamage, K., and Makino, S. (2009) Suppression of host gene expression by nsp1 proteins of group 2 bat coronaviruses. *J. Virol.* **83,** 5282–5288
10. Peiris, J. S., Guan, Y., and Yuen, K. Y. (2004) Severe acute respiratory syndrome. *Nat. Med.* **10,** S88–S97
11. Cavanagh, D. (2005) Coronaviruses in poultry and other birds. *Avian Pathol.* **34,** 439–448
12. Sawicki, S. G., Sawicki, D. L., and Siddell, S. G. (2007) A contemporary view of coronavirus transcription. *J. Virol.* **81,** 20–29
13. van Hemert, M. J., van den Worm, S. H., Knoops, K., Mommaas, A. M., Gorbalenya, A. E., and Snijder, E. J. (2008) SARS-coronavirus replication/transcription complexes are membrane-protected and need a host factor for activity in vitro. *PLoS Pathog.* **4,** e1000054
14. Prentice, E., Jerome, W. G., Yoshimori, T., Mizushima, N., and Denison, M. R. (2004) Coronavirus replication complex formation utilizes components of cellular autophagy. *J. Biol. Chem.* **279,** 10136–10141
15. de Haan, C. A., and Reggiori, F. (2008) Are nidoviruses hijacking the autophagy machinery? *Autophagy* **4,** 276–279
16. Bost, A. G., Prentice, E., and Denison, M. R. (2001) Mouse hepatitis virus replicase protein complexes are translocated to sites of M protein accumulation in the ERGIC at late times of infection. *Virology* **285,** 21–29
17. Cawood, R., Harrison, S. M., Dove, B. K., Reed, M. L., and Hiscox, J. A. (2007) Cell cycle dependent nucleolar localization of the coronavirus nucleocapsid protein. *Cell Cycle* **6,** 863–867
18. Freundt, E. C., Yu, L., Park, E., Lenardo, M. J., and Xu, X. N. (2009) Molecular determinants for subcellular localization of the severe acute respiratory syndrome coronavirus open reading frame 3b protein. *J. Virol.* **83,** 6631–6640
19. Spencer, K. A., Dee, M., Britton, P., and Hiscox, J. A. (2008) Role of phosphorylation clusters in the biology of the coronavirus infectious bronchitis virus nucleocapsid protein. *Virology* **370,** 373–381
20. Spencer, K. A., and Hiscox, J. A. (2006) Characterisation of the RNA binding properties of the coronavirus infectious bronchitis virus nucleocapsid protein amino-terminal region. *FEBS Lett.* **580,** 5993–5998
21. Chen, H., Gill, A., Dove, B. K., Emmett, S. R., Kemp, C. F., Ritchie, M. A., Dee, M., and Hiscox, J. A. (2005) Mass spectroscopic characterisation of the coronavirus infectious bronchitis virus nucleoprotein and elucidation of the role of phosphorylation in RNA binding using surface plasmon resonance. *J. Virol.* **79,** 1164–1179
22. Zúñiga, S., Sola, I., Moreno, J. L., Sabella, P., Plana-Durán, J., and Enjuanes, L. (2007) Coronavirus nucleocapsid protein is an RNA chaperone. *Virology* **357,** 215–227
23. Hiscox, J. A. (2007) RNA viruses: hijacking the dynamic nucleolus. *Nat. Rev. Microbiol.* **5,** 119–127
24. Hiscox, J. A. (2002) Brief review: the nucleolus—a gateway to viral infection? *Arch. Virol.* **147,** 1077–1089
25. Greco, A. (2009) Involvement of the nucleolus in replication of human viruses. *Rev. Med. Virol.* **19,** 201–214
26. Jiang, X. S., Tang, L. Y., Dai, J., Zhou, H., Li, S. J., Xia, Q. C., Wu, J. R., and Zeng, R. (2005) Quantitative analysis of severe acute respiratory syndrome (SARS)-associated coronavirus-infected cells using proteomic approaches: implications for cellular responses to virus infection. *Mol. Cell. Proteomics* **4,** 902–913
27. Yount, B., Curtis, K. M., Fritz, E. A., Hensley, L. E., Jahrling, P. B., Prentice, E., Denison, M. R., Geisbert, T. W., and Baric, R. S. (2003) Reverse genetics with a full-length infectious cDNA of severe acute respiratory syndrome coronavirus. *Proc. Natl. Acad. Sci. U.S.A.* **100,** 12995–13000
28. Batonick, M., Oomens, A. G., and Wertz, G. W. (2008) Human respiratory syncytial virus glycoproteins are not required for apical targeting and release from polarized epithelial cells. *J. Virol.* **82,** 8664–8672
29. Dauber, B., Heins, G., and Wolff, T. (2004) The influenza B virus nonstructural NS1 protein is essential for efficient viral growth and antagonizes beta interferon induction. *J. Virol.* **78,** 1865–1872
30. Carlos, T. S., Young, D. F., Schneider, M., Simas, J. P., and Randall, R. E. (2009) Parainfluenza virus 5 genomes are located in viral cytoplasmic bodies whilst the virus dismantles the interferon-induced antiviral state of cells. *J. Gen. Virol.* **90,** 2147–2156
31. Molestina, R. E., and Sinai, A. P. (2005) Host and parasite-derived IKK activities direct distinct temporal phases of NF-kappaB activation and

target gene expression following Toxoplasma gondii infection. *J. Cell Sci.* **118,** 5785–5796
32. Hsu, J. T., Kuo, C. J., Hsieh, H. P., Wang, Y. C., Huang, K. K., Lin, C. P., Huang, P. F., Chen, X., and Liang, P. H. (2004) Evaluation of metal-conjugated compounds as inhibitors of 3CL protease of SARS-CoV. *FEBS Lett.* **574,** 116–120
33. Keitel, W. A., Dekker, C. L., Mink, C., Campbell, J. D., Edwards, K. M., Patel, S. M., Ho, D. Y., Talbot, H. K., Guo, K., Noah, D. L., and Hill, H. (2009) Safety and immunogenicity of inactivated, Vero cell culture-derived whole virus influenza A/H5N1 vaccine given alone or with aluminum hydroxide adjuvant in healthy adults. *Vaccine* **27,** 6642–6648
34. Andersen, J. S., Lyon, C. E., Fox, A. H., Leung, A. K., Lam, Y. W., Steen, H., Mann, M., and Lamond, A. I. (2002) Directed proteomic analysis of the human nucleolus. *Curr. Biol.* **12,** 1–11
35. Shevchenko, A., Wilm, M., Vorm, O., and Mann, M. (1996) Mass spectrometric sequencing of proteins silver-stained polyacrylamide gels. *Anal. Chem.* **68,** 850–858
36. Olsen, J. V., de Godoy, L. M., Li, G., Macek, B., Mortensen, P., Pesch, R., Makarov, A., Lange, O., Horning, S., and Mann, M. (2005) Parts per million mass accuracy on an Orbitrap mass spectrometer via lock mass injection into a C-trap. *Mol. Cell. Proteomics* **4,** 2010–2021
37. Cox, J., and Mann, M. (2008) MaxQuant enables high peptide identification rates, individualized p.p.b.-range mass accuracies and proteome-wide protein quantification. *Nat. Biotechnol.* **26,** 1367–1372
38. Emmott, E., Dove, B. K., Howell, G., Chappell, L. A., Reed, M. L., Boyne, J. R., You, J. H., Brooks, G., Whitehouse, A., and Hiscox, J. A. (2008) Viral nucleolar localisation signals determine dynamic trafficking within the nucleolus. *Virology* **380,** 191–202
39. Mann, M. (2006) Functional and quantitative proteomics using SILAC. *Nat. Rev. Mol. Cell Biol.* **7,** 952–958
40. Skiba, M., Mettenleiter, T. C., and Karger, A. (2008) Quantitative whole-cell proteome analysis of pseudorabies virus-infected cells. *J. Virol.* **82,** 9689–9699
41. Li, D., and Cavanagh, D. (1992) Coronavirus IBV-induced membrane fusion occurs at near-neutral pH. *Arch. Virol.* **122,** 307–316
42. Fang, X., Gao, J., Zheng, H., Li, B., Kong, L., Zhang, Y., Wang, W., Zeng, Y., and Ye, L. (2007) The membrane protein of SARS-CoV suppresses NF-kappaB activation. *J. Med. Virol.* **79,** 1431–1439
43. Wang, W., Ye, L., Ye, L., Li, B., Gao, B., Zeng, Y., Kong, L., Fang, X., Zheng, H., Wu, Z., and She, Y. (2007) Up-regulation of IL-6 and TNF-alpha induced by SARS-coronavirus spike protein in murine macrophages via NF-kappaB pathway. *Virus Res.* **128,** 1–8
44. Kopecky-Bromberg, S. A., Martínez-Sobrido, L., Frieman, M., Baric, R. A., and Palese, P. (2007) Severe acute respiratory syndrome coronavirus open reading frame (ORF) 3b, ORF 6, and nucleocapsid proteins function as interferon antagonists. *J. Virol.* **81,** 548–557
45. Shaulian, E., and Karin, M. (2002) AP-1 as a regulator of cell life and death. *Nat. Cell Biol.* **4,** E131–E136
46. Parcellier, A., Schmitt, E., Gurbuxani, S., Seigneurin-Berny, D., Pance, A., Chantôme, A., Plenchette, S., Khochbin, S., Solary, E., and Garrido, C. (2003) HSP27 is a ubiquitin-binding protein involved in I-kappaBalpha proteasomal degradation. *Mol. Cell. Biol.* **23,** 5790–5802
47. De, A. K., Kodys, K. M., Yeh, B. S., and Miller-Graziano, C. (2000) Exaggerated human monocyte IL-10 concomitant to minimal TNF-alpha induction by heat-shock protein 27 (Hsp27) suggests Hsp27 is primarily an antiinflammatory stimulus. *J. Immunol.* **165,** 3951–3958
48. Alford, K. A., Glennie, S., Turrell, B. R., Rawlinson, L., Saklatvala, J., and Dean, J. L. (2007) Heat shock protein 27 functions in inflammatory gene expression and transforming growth factor-beta-activated kinase-1 (TAK1)-mediated signaling. *J. Biol. Chem.* **282,** 6232–6241
49. Aschenbrenner, L., Lee, T., and Hasson, T. (2003) Myo6 facilitates the translocation of endocytic vesicles from cell peripheries. *Mol. Biol. Cell* **14,** 2728–2743
50. Hertzano, R., Shalit, E., Rzadzinska, A. K., Dror, A. A., Song, L., Ron, U., Tan, J. T., Shitrit, A. S., Fuchs, H., Hasson, T., Ben-Tal, N., Sweeney, H. L., de Angelis, M. H., Steel, K. P., and Avraham, K. B. (2008) A Myo6 mutation destroys coordination between the myosin heads, revealing new functions of myosin VI in the stereocilia of mammalian inner ear hair cells. *PLoS Genet.* **4,** e1000207
51. Dove, B. K., You, J. H., Reed, M. L., Emmett, S. R., Brooks, G., and Hiscox, J. A. (2006) Changes in nucleolar morphology and proteins during infection with the coronavirus infectious bronchitis virus. *Cell. Microbiol.* **8,** 1147–1157
52. Lam, Y. W., Evans, V. C., Heesom, K. J., Lamond, A. I., and Matthews, D. A. (2010) Proteomics analysis of the nucleolus in adenovirus-infected cells. *Mol. Cell. Proteomics* **9,** 117–130
53. Mannová, P., Fang, R., Wang, H., Deng, B., McIntosh, M. W., Hanash, S. M., and Beretta, L. (2006) Modification of host lipid raft proteome upon hepatitis C virus replication. *Mol. Cell. Proteomics* **5,** 2319–2325
54. Brasier, A. R., Spratt, H., Wu, Z., Boldogh, I., Zhang, Y., Garofalo, R. P., Casola, A., Pashmi, J., Haag, A., Luxon, B., and Kurosky, A. (2004) Nuclear heat shock response and novel nuclear domain 10 reorganization in respiratory syncytial virus-infected A549 cells identified by high-resolution two-dimensional gel electrophoresis. *J. Virol.* **78,** 11461–11476
55. Zheng, X., Hong, L., Shi, L., Guo, J., Sun, Z., and Zhou, J. (2008) Proteomics analysis of host cells infected with infectious bursal disease virus. *Mol. Cell. Proteomics* **7,** 612–625
56. Pattanakitsakul, S. N., Rungrojcharoenkit, K., Kanlaya, R., Sinchaikul, S., Noisakran, S., Chen, S. T., Malasit, P., and Thongboonkerd, V. (2007) Proteomic analysis of host responses in HepG2 cells during dengue virus infection. *J. Proteome Res.* **6,** 4592–4600
57. Reed, M. L., Dove, B. K., Jackson, R. M., Collins, R., Brooks, G., and Hiscox, J. A. (2006) Delineation and modelling of a nucleolar retention signal in the coronavirus nucleocapsid protein. *Traffic* **7,** 833–848
58. Reed, M. L., Howell, G., Harrison, S. M., Spencer, K. A., and Hiscox, J. A. (2007) Characterization of the nuclear export signal in the coronavirus infectious bronchitis virus nucleocapsid protein. *J. Virol.* **81,** 4298–4304
59. Hiscox, J. A., Wurm, T., Wilson, L., Britton, P., Cavanagh, D., and Brooks, G. (2001) The coronavirus infectious bronchitis virus nucleoprotein localizes to the nucleolus. *J. Virol.* **75,** 506–512
60. Wurm, T., Chen, H., Hodgson., T, Britton, P., Brooks, G., and Hiscox, J. A. (2001) Localisation to the nucleolus is a common feature of coronavirus nucleoproteins and the protein may disrupt host cell division. *J. Virol.* **75,** 9345–9356
61. Chen, H., Wurm, T., Britton, P., Brooks, G., and Hiscox, J. A. (2002) Interaction of the coronavirus nucleoprotein with nucleolar antigens and the host cell. *J. Virol.* **76,** 5233–5250
62. Corse, E., and Machamer, C. E. (2003) The cytoplasmic tails of infectious bronchitis virus E and M proteins mediate their interaction. *Virology* **312,** 25–34
63. Corse, E., and Machamer, C. E. (2000) Infectious bronchitis virus E protein is targeted to the Golgi complex and directs release of virus-like particles. *J. Virol.* **74,** 4319–4326
64. Frieman, M., Ratia, K., Johnston, R. E., Mesecar, A. D., and Baric, R. S. (2009) Severe acute respiratory syndrome coronavirus papain-like protease ubiquitin-like domain and catalytic domain regulate antagonism of IRF3 and NF-kappaB signaling. *J. Virol.* **83,** 6689–6705
65. Chang, Y. J., Liu, C. Y., Chiang, B. L., Chao, Y. C., and Chen, C. C. (2004) Induction of IL-8 release in lung cells via activator protein-1 by recombinant baculovirus displaying severe acute respiratory syndrome-coronavirus spike proteins: identification of two functional regions. *J. Immunol.* **173,** 7602–7614
66. He, R., Leeson, A., Andonov, A., Li, Y., Bastien, N., Cao, J., Osiowy, C., Dobie, F., Cutts, T., Ballantine, M., and Li, X. (2003) Activation of AP-1 signal transduction pathway by SARS coronavirus nucleocapsid protein. *Biochem. Biophys. Res. Commun.* **311,** 870–876
67. Shaulian, E., and Karin, M. (2001) AP-1 in cell proliferation and survival. *Oncogene* **20,** 2390–2400
68. Harrison, S. M., Dove, B. K., Rothwell, L., Kaiser, P., Tarpey, I., Brooks, G., and Hiscox, J. A. (2007) Characterisation of cyclin D1 down-regulation in coronavirus infected cells. *FEBS Lett.* **581,** 1275–1286
69. Lavi, E., Wang, Q., Weiss, S. R., and Gonatas, N. K. (1996) Syncytia formation induced by coronavirus infection is associated with fragmentation and rearrangement of the Golgi apparatus. *Virology* **221,** 325–334
70. Kalicharran, K., and Dales, S. (1996) The murine coronavirus as a model of trafficking and assembly of viral proteins in neural tissue. *Trends Microbiol.* **4,** 264–269
71. Wang, J., Fang, S., Xiao, H., Chen, B., Tam, J. P., and Liu, D. X. (2009) Interaction of the coronavirus infectious bronchitis virus membrane protein with beta-actin and its implication in virion assembly and budding. *PLoS One* **4,** e4908

72. Vreugde, S., Ferrai, C., Miluzio, A., Hauben, E., Marchisio, P. C., Crippa, M. P., Bussi, M., and Biffo, S. (2006) Nuclear myosin VI enhances RNA polymerase II-dependent transcription. *Mol. Cell* **23,** 749–755
73. Jung, E. J., Liu, G., Zhou, W., and Chen, X. (2006) Myosin VI is a mediator of the p53-dependent cell survival pathway. *Mol. Cell. Biol.* **26,** 2175–2186
74. Bhattacharya, B., Noad, R. J., and Roy, P. (2007) Interaction between Bluetongue virus outer capsid protein VP2 and vimentin is necessary for virus egress. *Virol. J.* **4,** 7
75. Chen, W., Gao, N., Wang, J. L., Tian, Y. P., Chen, Z. T., and An, J. (2008) Vimentin is required for dengue virus serotype 2 infection but microtubules are not necessary for this process. *Arch. Virol.* **153,** 1777–1781
76. Stefanovic, S., Windsor, M., Nagata, K. I., Inagaki, M., and Wileman, T. (2005) Vimentin rearrangement during African swine fever virus infection involves retrograde transport along microtubules and phosphorylation of vimentin by calcium calmodulin kinase II. *J. Virol.* **79,** 11766–11775
77. Risco, C., Rodríguez, J. R., López-Iglesias, C., Carrascosa, J. L., Esteban, M., and Rodríguez, D. (2002) Endoplasmic reticulum-Golgi intermediate compartment membranes and vimentin filaments participate in vaccinia virus assembly. *J. Virol.* **76,** 1839–1855
78. Emmott, E., and Hiscox, J. A. (2009) Nucleolar targetting: the hub of the matter. *EMBO Rep.* **10,** 231–238
79. Salsman, J., Zimmerman, N., Chen, T., Domagala, M., and Frappier, L. (2008) Genome-wide screen of three herpesviruses for protein subcellular localization and alteration of PML nuclear bodies. *PLoS Pathog.* **4,** e1000100
80. Boyne, J. R., and Whitehouse, A. (2006) Nucleolar trafficking is essential for nuclear export of intronless herpesvirus mRNA. *Proc. Natl. Acad. Sci. U.S.A.* **103,** 15190–15195
81. Lymberopoulos, M. H., and Pearson, A. (2007) Involvement of UL24 in herpes-simplex-virus-1-induced dispersal of nucleolin. *Virology* **363,** 397–409
82. Callé, A., Ugrinova, I., Epstein, A. L., Bouvet, P., Diaz, J. J., and Greco, A. (2008) Nucleolin is required for an efficient herpes simplex virus type 1 infection. *J. Virol.* **82,** 4762–4773
83. Matthews, D. A. (2001) Adenovirus protein V induces redistribution of nucleolin and B23 from nucleolus to cytoplasm. *J. Virol.* **75,** 1031–1038
84. Lawrence, F. J., McStay, B., and Matthews, D. A. (2006) Nucleolar protein upstream binding factor is sequestered into adenovirus DNA replication centres during infection without affecting RNA polymerase I location or ablating rRNA synthesis. *J. Cell Sci.* **119,** 2621–2631
85. Enjuanes, L., Almazán, F., Sola, I., and Zuñiga, S. (2006) Biochemical aspects of coronavirus replication and virus-host interaction. *Annu. Rev. Microbiol.* **60,** 211–230